Front. Earth Sci. 2018, 12(1): 191–214
https://doi.org/10.1007/s11707-016-0623-y

RESEARCH ARTICLE

Late Paleozoic-Early Mesozoic tectonic evolution of the Paleo-Asian Ocean: geochronological and geochemical evidence from granitoids in the northern margin of Alxa, Western China

Xin SHA[1], Jinrong WANG (✉)[1], Wanfeng CHEN[1], Zheng LIU[1,2], Xinwei ZHAI[1], Jinlong MA[1], Shuhua WANG[1]

1 School of Earth Sciences, Gansu Key Laboratory of Mineral Resources in Western China Lanzhou University, Lanzhou 730000, China
2 State Key Laboratory for Mineral Deposits Research, Nanjing University, Nanjing 210000, China

Abstract The Paleo-Asian Ocean (Southern Mongolian Ocean) ophiolitic belts and massive granitoids are exposed in the Alxa block, in response to oceanic subduction processes. In this work, we report petrographic, geochemical, and zircon U-Pb age data of some granitoid intrusions from the northern Alxa. Zircon U-Pb dating for the quartz diorite, tonalite, monzogranite, and biotite granite yielded weighted mean $^{206}Pb/^{238}U$ ages of 302±9.2 Ma, 246.5±4.6 Ma, 235±4.4 Ma, and 229.5±5.6 Ma, respectively. The quartz diorites (~302 Ma) exhibit geochemical similarities to adakites, likely derived from partial melting of the initially subducted Chaganchulu back-arc oceanic slab. The tonalites (~246.5 Ma) display geochemical affinities of I-type granites. They were probably derived by fractional crystallization of the modified lithospheric mantle-derived basaltic magmas in a volcanic arc setting. The monzogranites (~235 Ma) are characterized by low Al_2O_3, but high Y and Yb with notably negative Eu anomalies. In contrast, the biotite granites (~229.5 Ma) show high Al_2O_3 but low Y and Yb with steep HREE patterns and the absence of negative Eu anomalies. Elemental data suggested that the biotite granites were likely derived from a thickened lower crust, but the monzogranites originated from a thin crust. Our data suggested that the initial subduction of the Chaganchulu oceanic slab towards the Alxa block occurred at ~ 302 Ma. This subduction process continued to the Early Triassic (~246 Ma) and the basin was finally closed before the Middle Triassic (~235 Ma). Subsequently, the break-off of the subducted slab triggered asthenosphere upwelling (240–230 Ma).

Received January 6, 2016; accepted October 9, 2016

E-mail: jrwang@lzu.edu.cn

Keywords Paleo-Asian Ocean, Alxa, granite, geochemistry

1 Introduction

The Alxa block occupies a key tectonic position at the junction between the Central Asian Orogenic Belt (CAOB), the Tarim block, the North China Craton and the North Qilian orogenic belt (Wu and He, 1993; Wang et al., 1994; Zhang et al., 1997; Zhai and Bian, 2000; Ge et al., 2009; Geng and Zhou, 2012; Gong et al., 2012, 2013; Song et al., 2013; Zhang et al., 2013). The northern margin of the Alxa block is attached to the southern CAOB which is one of the most important areas for studying Phanerozoic continental growth in the world (Fig. 1). The Alxa block is a critical zone to investigate the tectonic evolution of the Paleo-Asian Ocean. There was a general consensus that successive lateral accretions from the Paleo-Asian Ocean produced the CAOB, with the formation of abundant accretionary complexes. However, the time of the closure of the Paleo-Asian Ocean remained controversial: 1) before late Carboniferous (Gao et al., 1998; Chen et al., 1999; Gao and Klemd, 2003; Xia et al., 2004; Charvet et al., 2007, 2011; Wang et al., 2007a, 2011; Gao et al., 2009; Yang and Zhou, 2009; Han et al., 2010a, b, c, 2011; Hegner et al., 2010); 2) in the late Permian-early Triassic (Li et al., 2002, 2005; Li et al., 2009; Xiao et al., 2008, 2009, 2010a, b, 2013, 2015; Tian et al., 2013, 2015) and 3) during the Triassic (Zhang et al., 2005; Zhang et al., 2007). Most studies have focused on three regions: the northern part of Xinjiang, Mongolia, and the eastern border of Mongolia (Fig. 1) including the Altai orogenic belt (Vladimirov et al., 2001, 2005; Annikova et al., 2006; Wang et al., 2007c, 2008a), the eastern Tianshan orogenic belt (Wang et al., 2008b; Zhou et al., 2010), the Hegenshan orogen and the Suolunshan-Xilamulun regions at the eastern border of Mongolia (Tao et al., 2003; Shi et al., 2004; Bao et al., 2007; Li et al., 2007; Zhao et al., 2007; Miao et al., 2008; Zhang et al., 2008; Chen et al., 2009; Liu et al., 2009; Zhang, 2009; Tong et al., 2010a, b), and the Northern Mongolia-West Baikal orogenic belt (Yarmolyuk et al., 2002; Jahn et al., 2009). However, only a few studies have been carried out in the northern Alxa block (Wang et al., 1998a, b; Xu et al., 2001; Zhang et al., 2002b; Wang et al., 2004; Li et al., 2010; Zhang et al., 2013; Zheng et al., 2014) and western Inner Mongolia (Li et al., 2006a; Wang et al., 2010; Zhang et al., 2011; Li et al., 2012).

In this work, LA-ICP-MS zircon U-Pb dating and major and trace element geochemical data have been determined for some felsic intrusions in the northern Alxa block. Our main objectives are to reconstruct the tectonic framework of the Alxa from late Paleozoic to early Mesozoic and to further constraint the closure of the Paleo-Asian Ocean.

2 Geological setting

The Alxa block includes three important boundary faults and two ophiolitic belts. The three faults from north to south are the Yagan fault belt, the Wutaohai-Enger Us fault belt, and the Chaganchulu fault belt (the Badanjilin fault belt, Zheng et al., 2014) (Fig. 2). The northern margin of the Alxa can be further divided into four tectonic units by the three faults (Fig. 2; Wu and He, 1993): the Yagan tectonic belt (immature island arc), the Zhusileng-Hangwula Paleozoic tectonic belt (early Paleozoic passive continental margin that converted to an active continental margin in the late Paleozoic), the Zongnaishan-Shalazhashan tectonic belt (mature island arc), and the Bayinnuoergong-Langshan tectonic belt (stable block).

The Zhusileng-Hangwula tectonic belt is located between the Yagan fault belt and the Enger Us fault belt. The Precambrian strata include metarhyolite, slate, quartzite, and granitic gneiss. Dalmanitina fossils are discovered in the Ordovician strata. Wu and He (1993) suggested that the tectonic belt represented an early Paleozoic passive continental margin. In addition, the lower Paleozoic strata were mainly carbonate-flysch formations and submarine volcanics. These observations indicated that the Zhusileng-Hangwula tectonic belt transformed from a passive continental margin to an active continental margin in the late Paleozoic (Wu and He, 1993).

The Zongnaishan-Shalazhashan tectonic belt is bounded by the Enger Us fault belt to the south and the Chaganchulu fault belt to the north. The ancient strata are Mesoarchean-Paleoproterozoic strata comprising the Alxa Group metamorphic rocks (Wang et al., 1994). In addition, Paleozoic to Mesozoic granitoids widely occurred in the belt, such as the Zongnaishan granite (single zircon U-Pb ages of 236.6±0.95 Ma, 249.7±2.6 Ma, and 268.4±0.69 Ma) which was interpreted to be a continental margin arc granite (Xie et al., 2014). However, as the principal part of the Zongnaishan-Shalazhashan arc zone, the Wuliji granite (~250.8 Ma) was interpreted to be a post-collisional granite and was produced by partial melting of mantle with assimilation of volcanic arc crust (Zhang et al., 2013).

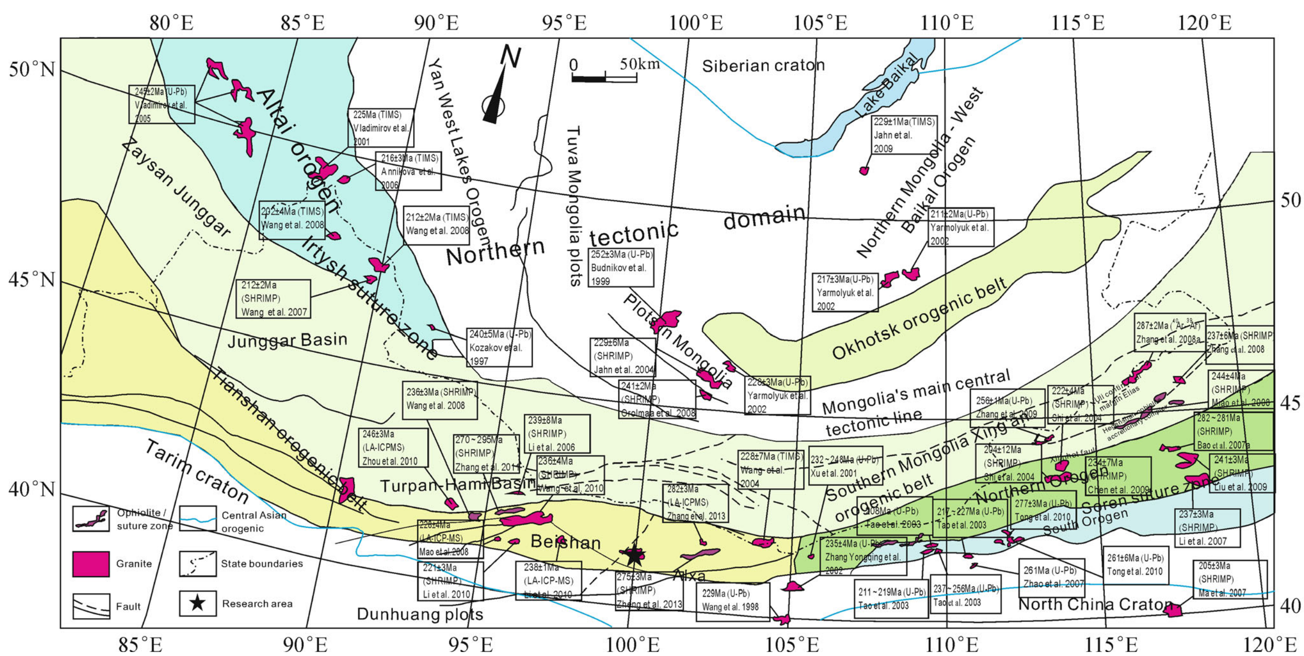

Fig. 1 Distribution of Early Mesozoic granitoids in the middle-south segment of the CAOB (modified after Li et al., 2010; Tong et al., 2010a; Li et al., 2012).

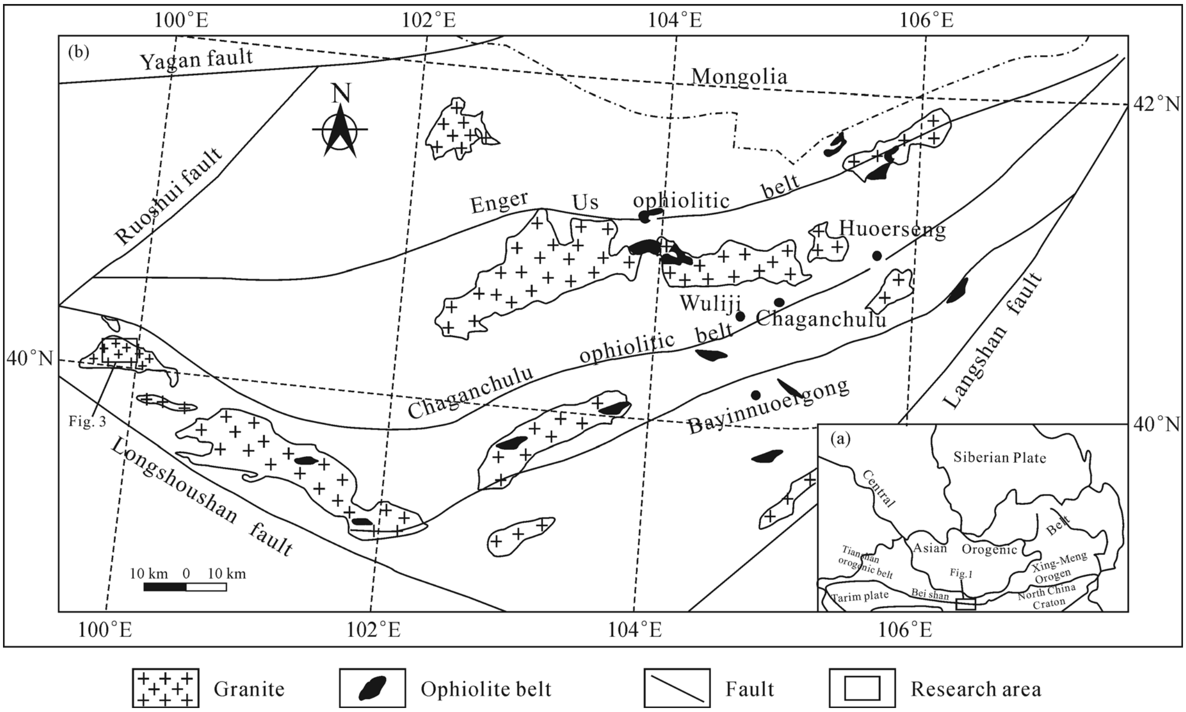

Fig. 2 The sketch of plate tectonic units in the Alxa block.

Based on these published data, the Zongnaishan-Shalazhashan tectonic belt was considered as a volcanic arc (Zhang et al., 2013; Xie et al., 2014; Zheng et al., 2014).

In the Bayinnuoergong-Langshan tectonic belt the Precambrian basement are mainly composed of metasedimentary and metavolcanic rocks, and tonalitic-granodioritic gneisses (Geng et al., 2007; Geng and Zhou, 2010, 2011). Abundant Permian granites (289–269 Ma) occurred in this belt, including dioritic gneiss, garnet-bearing tonalitic gneisses, and gneissic granites. They exhibit crust-mantle mixed geochemical characteristics (Geng and Zhou, 2012). Additionally, the Bayinnuoergong granite (zircon U-Pb age of 252.3$\pm$0.96 Ma) has been interpreted to be a syn-collisional granite (Xie et al., 2014).

Two ophiolitic belts (Enger Us and Chaganchulu) have been discussed in previous studies (e.g., Zheng et al., 2014). The Enger Us ophiolitic belt extended in NEE direction. The Enger Us ophiolitic suite consisted of ultrabasic rocks, gabbros, basalts, and cherts (Wang et al., 1994). Most of the mafic-ultramafic rocks were highly deformed and had undergone carbonatation and silicification. The Chaganchulu ophiolitic belt consisted of lenticular and striped ultrabasic rocks, gabbros, cherts, and rare basalts (Wang et al., 1994; Zheng et al., 2014). Based on regional geology, paleobiogeography, paleomagnetic and geochemical evidence, Zheng et al. (2014) suggested that the Enger Us ophiolitic belt represented the Paleo-Asian major oceanic basin and the Chaganchulu ophiolitic belt represented a back-arc basin. Recently, Zhang et al. (2015) have carried out statistical analysis of zircon xenocrysts within Permian magmatic rocks from the Zongnaishan-Shalazhashan (ZS) tectonic belt and Bayinnuoergong-Langshan (BL) tectonic belt. The ages and Hf isotopic data of the zircon xenocrysts imply that the basement beneath the ZS tectonic belt is relatively young, resembling the southern Central Asian Orogenic Belt (CAOB), in contrast to the BL tectonic belt. Thus, the boundary of the CAOB with the Alxa Block might be represented by the Chaganchulu ophiolitic belt.

3 Geology of granitoids and sampling

3.1 Quartz diorite

The quartz diorite is exposed in the Shazaoquan area (Fig. 3; samples AYQ-25, AYQ-26, AYQ-27, AYQ-28, and AYQ-29). It is intruded into the Lower Proterozoic Longshoushan Group. The quartz diorite was intruded by late biotite granite. The mineral assemblage consists of quartz (10%), plagioclases (55%), and amphiboles (35%). Accessory minerals include sphene and minor magnetite (Fig. 4(a)).

3.2 Tonalite

The tonalite is exposed in the Dashankou-Yaoquan area. It intruded into the quartz diorite and its middle section was later invaded by a Middle Triassic monzogranite (Fig. 3; samples AYQ-3, YQ-26, YQ-27, YQ-28, and YQ-29). It

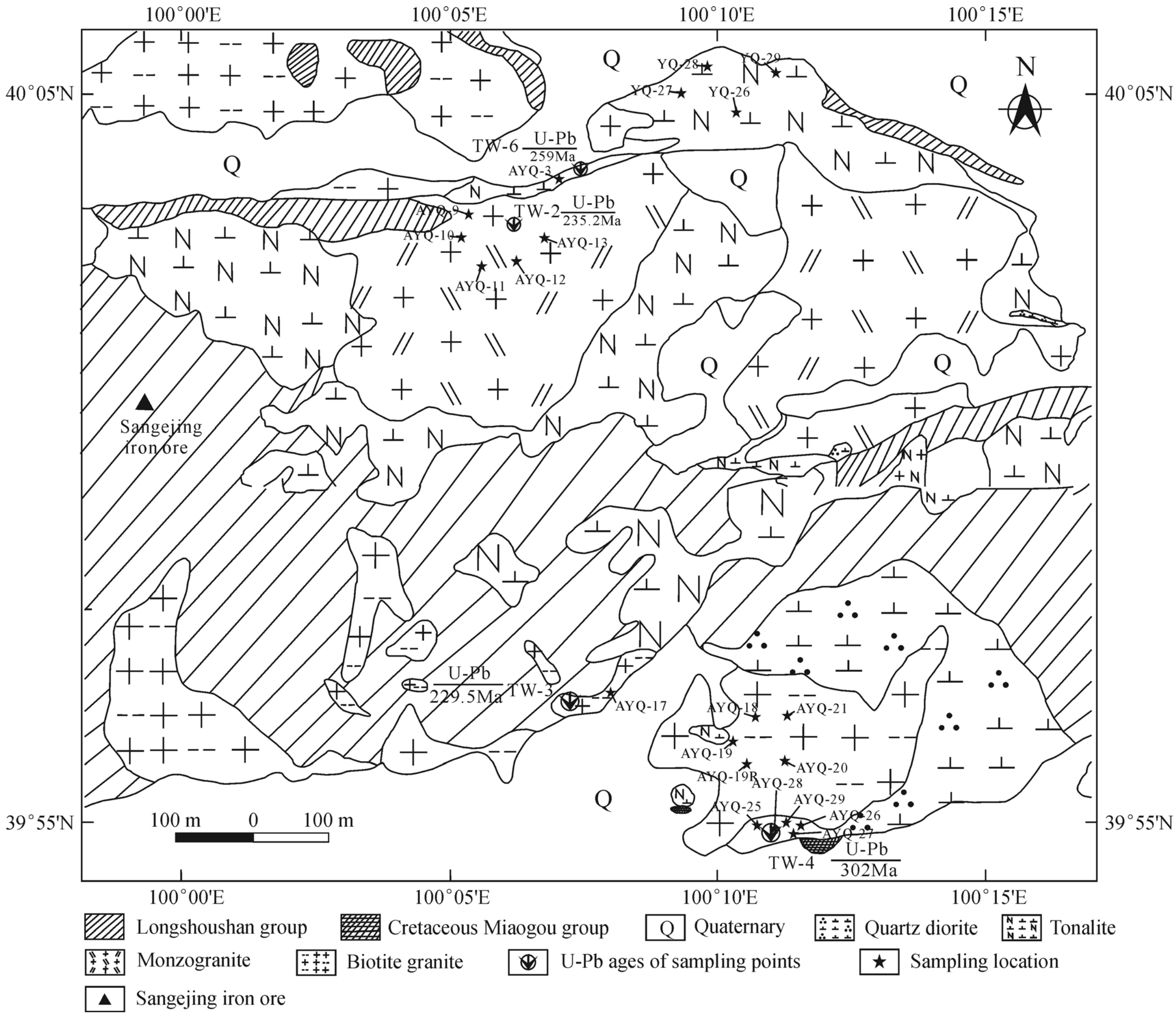

Fig. 3 Sketch of the rock block and location of samples.

consists mainly of quartz (25%), plagioclase (60%), biotite (8%), amphibole (5%), and secondary apatite and magnetite (Fig. 4(b)).

3.3 Monzogranite

The monzogranite is distributed in the Yaoquan-Hongshanliang area. Its irregular shape has its long axis extending in the EW direction, and it invaded the Paleoproterozoic Longshoushan Group and the Carboniferous quartz diorite (Fig. 3; samples AYQ-9, AYQ-10, AYQ-11, AYQ-12, and AYQ-13). It consists mainly of plagioclases (30%), other feldspars (33%), quartz (30%), and biotite (5%), with a small amount of opaque minerals (Fig. 4(c)).

3.4 Biotite granite

The biotite granite is located in western of the quartz diorite, and it invaded in the Paleoproterozoic Longshoushan Group (Fig. 3; samples AYQ-17, AYQ-18, AYQ-19, AYQ-19R, AYQ-20, AYQ-21). It consists mainly of quartz (30%), plagioclases (25%), other feldspars (42%), and biotite (3%) (Fig. 4(d)).

4 Analytical methods

Whole rock major elements were analyzed at the State Key Laboratory of Continental Dynamics, Northwest University, and were completed by the Rigaku RIX2100 X-ray fluorescence spectrometer (XRF), following the analytical procedures of Liu et al. (2007). The analytical precision is within 0.1%. Trace elements were analyzed at the State Key Laboratory of Continental Dynamics, Northwest University, and the Institute of Geochemistry in Guangzhou. The analyses were completed using the Perkin-Elmer Sciex ELAN 6000 inductively coupled plasma mass spectrometer (Guangzhou) and the 820-MS plasma mass spectrometer (Northwest University), following the analy-

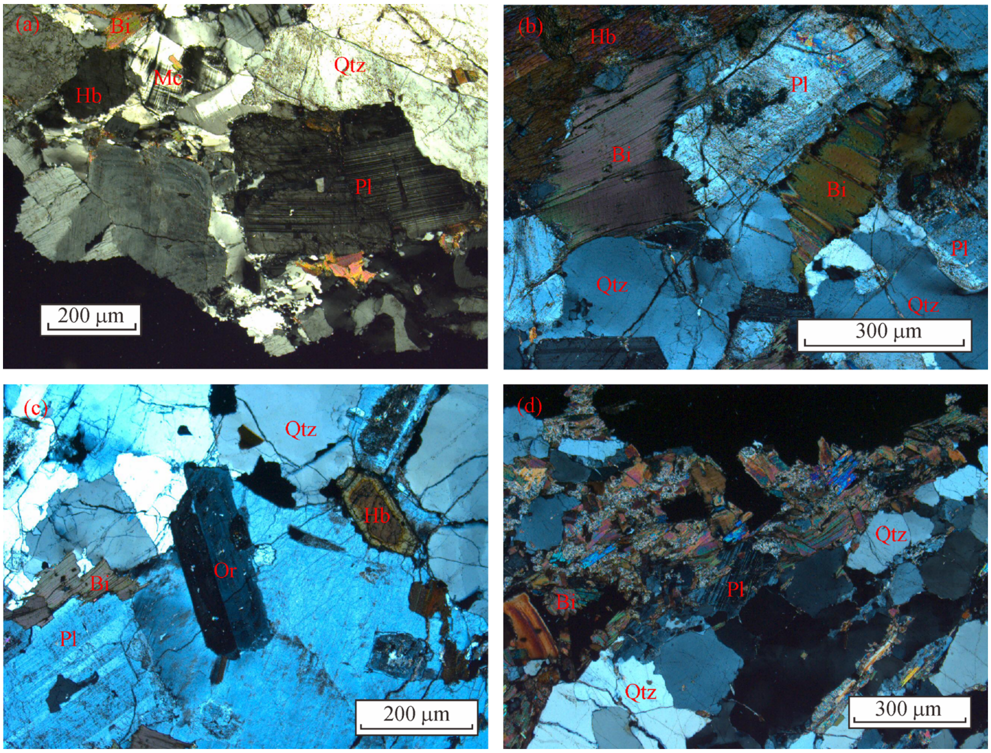

Fig. 4 Microphotographs of rocks. (a) Quartz diorite; (b) tonalite; (c) monzogranite; (d) biotite granite. Or: Orthoclase; Pl: Plagioclase; Bi: Biotite; Qtz: Quartz; Hb: Amphibole; Mc: Microcline.

tical procedures of Govindaraju (1994), Li (1997), and Li et al. (2006b). The analytical precision is within 5%. The results of these analyses are shown in Table 1.

Fresh rock samples were crushed to pass a 120-mesh sieve, and separation of zircon crystals was accomplished by conventional artificial panning, heavy liquid separation, magnetic techniques, and binocular microscope observation. Samples were numbered as quartz diorite (TW-4), tonalite (TW-6), monzogranite (TW-2), and biotite granite (TW-3). Zircon cathodoluminescence (CL) images and LA-ICP-MS zircon U-Pb dating were completed by the State Key Laboratory of Continental Dynamics, Northwest University. LA-ICP-MS was performed with the 820-MS plasma mass spectrometer, which has the collision response system and was the newest generation machine of Varian, Inc. (USA). The laser ablation system was the GeoLas 2005-type, ArF 193 nm UV excimer laser, which was produced by the Lambda Physik AG Company (Germany). The analytical procedures followed those of Liu et al. (2007). The analytical results are shown in Table 2.

5 Results

5.1 LA-ICP-MS zircon U-Pb dating

Zircons of the samples are mostly euhedral with short columnar shapes. The zircons display oscillatory zoning consistent with magmatic zircons (Fig. 5; Belousova et al., 2002). They exhibit wide ranges of U (31.89–4187.52 ppm) and Th (17.69–1440 ppm) contents with high Th/U ratios (0.16–1.43 ppm) typical of magmatic zircons (Belousova et al., 2002). Based on the fact that the ordinary lead correction can cause a greater effect on the $^{207}Pb/^{235}U$ ratio, we adopted the $^{206}Pb/^{238}U$ age-weighted average to represent the formation age of these granitoids. Zircon U-Pb dating results for the quartz diorite, tonalite, monzonitic granite, and biotite granites yielded weighted mean $^{206}Pb/^{238}U$ ages of 302±9.2 Ma, 246.5±4.6 Ma, 235±4.4 Ma, and 229±5.6 Ma, respectively (Fig. 6; Table 2).

5.2 Whole-rock geochemistry

5.2.1 Quartz diorite (~302 Ma)

The quartz diorites have SiO_2 contents ranging from 60.66 wt% to 61.37 wt% (Table 1). They exhibit relatively high Al_2O_3 (17.98–18.44 wt%), CaO (6.08–6.59 wt%), and Na_2O (4.20%–4.46 wt%), but low K_2O (0.67%–0.92 wt%). The MgO contents range from 2.13–2.51 wt% with variable Mg-number ($Mg^{\#}$) values of 48 to 51. The sample points plot in the low-K (tholeiitic) series of the SiO_2-K_2O diagram (Fig. 7(a)) and in the diorite field of the SiO_2-($Na_2O + K_2O$) discrimination diagram (Fig. 7(b)).

Table 1 Major-element and trace-element compositions of the granitoids

No. Rocks	AYQ-25 quartz diorite	AYQ-26 quartz diorite	AYQ-27 quartz diorite	AYQ-28 quartz diorite	AYQ-29 quartz diorite	AYQ-3 tonalite	YQ-26 tonalite	YQ-27 tonalite	YQ-28 tonalite	YQ-29 tonalite
SiO_2	60.99	60.66	61.05	61.10	61.37	62.14	67.93	68.94	67.04	66.83
Al_2O_3	17.98	18.16	18.41	18.44	18.42	16.97	16.55	16.12	16.26	16.60
TiO_2	0.58	0.63	0.60	0.58	0.62	0.76	0.53	0.50	0.54	0.52
TFe_2O_3	4.81	5.13	4.74	4.66	4.59	5.11	3.24	3.26	3.81	3.40
MnO	0.10	0.09	0.09	0.09	0.08	0.08	0.07	0.07	0.07	0.05
MgO	2.51	2.51	2.32	2.31	2.13	2.30	1.29	1.15	1.33	1.40
CaO	6.52	6.08	6.42	6.40	6.59	4.84	2.89	2.53	3.14	3.53
Na_2O	4.32	4.20	4.46	4.28	4.26	3.69	4.30	4.28	4.26	4.30
K_2O	0.67	0.92	0.76	0.76	0.70	2.66	2.14	2.43	2.52	2.44
P_2O_5	0.18	0.18	0.18	0.18	0.18	0.26	0.16	0.15	0.17	0.17
LOI	0.84	0.97	0.57	0.74	0.64	0.69	0.84	0.83	1.22	1.16
Total	99.50	99.53	99.60	99.54	99.58	99.50	100.2	100.4	100.3	100.2
$Mg^{\#}$	51	49	49	50	48	47	44	41	41	45
Na_2O/K_2O	6.45	4.57	5.87	5.63	6.09	1.39	2.01	1.76	1.69	1.76
A/CNK	0.91	0.96	0.93	0.94	0.93	0.95	1.13	1.13	1.05	1.03
σ	1.38	1.48	1.51	1.40	1.34	2.11	1.66	1.74	1.91	1.91
Ba	161	213	160	197	143	569	428	537	378	427
Rb	19	27	22	27	21	135	113	114	114	102
Cs	1.42	1.73	1.99	2.14	1.89	6.82	5.99	9.32	8.05	6.95
Th	1.31	2.30	1.88	3.98	1.59	8.98	13.7	12.2	10.7	11.4
U	0.70	0.69	0.30	0.45	0.92	3.04	2.11	1.95	1.61	2.09
Nb	4.00	4.52	4.29	4.02	4.32	13.31	12.9	13.6	13.1	15.6
Ta	0.26	0.29	0.28	0.26	0.33	1.35	0.98	1.11	1.04	2.35
K	5562	7637	6309	6309	5811	22082	17764	20171	20919	20255
Pb	6.48	6.67	6.66	6.60	6.91	16.60	19.4	19.1	15.7	14.5
Sr	587	582	611	607	620	457	362	333	358	428
Zr	95	93	102	103	76	265	205	220	198	231
Hf	2.53	2.34	2.47	2.48	1.92	6.01	4.88	5.37	4.77	5.53
P	786	786	786	786	786	1135	699	655	742	742
Ti	3476	3776	3596	3476	3716	4555	3177	2997	3236	3117
Y	16.72	13.70	13.20	11.41	12.83	22.72	25.3	31.3	24.7	60.0
Cr	16.84	16.42	14.24	13.35	16.03	31.19	23.1	18.2	18.8	19.3
Ni	10.88	11.55	10.33	10.59	10.62	12.18	7.87	6.48	6.83	7.58
La	11.01	12.25	12.70	15.44	12.18	19.08	47.9	43.1	37.6	32.5
Ce	26.21	27.44	27.71	31.05	25.40	40.56	91.3	87.0	72.1	68.3
Pr	3.56	3.47	3.41	3.57	3.17	4.97	10.3	9.55	7.88	8.19
Nd	16.18	14.77	14.38	14.25	13.54	20.89	37.6	33.5	28.4	33.1
Sm	3.76	3.15	3.02	2.74	2.89	4.79	6.92	5.74	5.45	8.61
Eu	1.17	1.07	1.07	1.02	1.05	1.25	0.96	0.97	0.94	1.39
Gd	3.49	2.84	2.73	2.43	2.65	4.54	6.04	5.01	5.00	8.86
Tb	0.51	0.40	0.39	0.34	0.38	0.66	0.84	0.84	0.76	1.69
Dy	2.97	2.36	2.26	1.99	2.21	3.86	4.56	5.30	4.42	11.0
Ho	0.58	0.46	0.45	0.39	0.44	0.75	0.83	1.05	0.85	2.18
Er	1.61	1.31	1.27	1.09	1.23	2.09	2.30	2.96	2.40	5.98

(*Continued*)

No. Rocks	AYQ-25 quartz diorite	AYQ-26 quartz diorite	AYQ-27 quartz diorite	AYQ-28 quartz diorite	AYQ-29 quartz diorite	AYQ-3 tonalite	YQ-26 tonalite	YQ-27 tonalite	YQ-28 tonalite	YQ-29 tonalite
Tm	0.23	0.19	0.19	0.16	0.18	0.31	0.32	0.41	0.35	0.81
Yb	1.51	1.22	1.20	1.02	1.16	2.00	2.13	2.50	2.30	4.57
Lu	0.22	0.19	0.18	0.16	0.17	0.29	0.31	0.36	0.34	0.56
ΣREE	73.15	71.12	70.96	75.65	66.65	106.0	212.2	198.3	168.7	187.6
Sr/Y	35.11	42.46	46.27	53.18	48.30	20.10	14.31	10.64	14.49	7.13
La/Yb	7.28	10.03	10.56	15.14	10.46	9.52	22.49	17.24	16.35	7.11
$(La/Yb)_N$	5.22	7.19	7.58	10.86	7.51	6.83	16.13	12.37	11.73	5.10
Y/Yb	11.05	11.21	10.98	11.19	11.02	11.33	11.88	12.52	10.74	13.13
Eu/Eu*	0.97	1.08	1.12	1.18	1.14	0.80	0.75	0.83	0.82	0.75
La/Ce	0.42	0.45	0.46	0.50	0.48	0.47	0.52	0.50	0.52	0.48
Rb/Sr	0.03	0.05	0.04	0.04	0.03	0.29	0.31	0.34	0.32	0.24
$(Gd/Yb)_N$	1.91	1.92	1.88	1.97	1.88	1.87	2.34	1.66	1.80	1.60

Table 1 (continued)

No. Rocks	AYQ-9 monzonitic granite	AYQ-10 monzonitic granite	AYQ-11 monzonitic granite	AYQ-12 monzonitic granite	AYQ-13 monzonitic granite	AYQ-17 biotite granite	AYQ-18 biotite granite	AYQ-19 biotite granite	AYQ-19R biotite granite	AYQ-20 biotite granite	AYQ-21 biotite granite
SiO_2	72.74	72.79	77.65	78.13	72.72	69.58	71.04	69.94	69.83	68.89	69.55
Al_2O_3	13.69	13.26	11.86	11.56	14.07	15.41	14.60	15.03	14.99	15.76	13.95
TiO_2	0.25	0.26	0.12	0.12	0.25	0.42	0.38	0.40	0.40	0.35	0.44
TFe_2O_3	2.00	1.88	1.04	1.12	1.92	2.76	2.62	2.80	2.80	2.41	2.80
MnO	0.05	0.04	0.03	0.03	0.04	0.05	0.04	0.04	0.04	0.04	0.04
MgO	0.56	0.55	0.20	0.21	0.52	0.76	0.72	0.73	0.73	0.63	0.81
CaO	1.76	2.32	1.10	0.93	1.64	2.13	2.08	1.87	1.85	1.75	2.54
Na_2O	3.80	3.74	3.46	3.15	3.57	3.87	3.92	3.64	3.63	3.64	4.81
K_2O	4.13	3.61	3.69	4.02	4.31	4.08	4.08	4.65	4.63	5.45	3.52
P_2O_5	0.09	0.08	0.04	0.04	0.08	0.13	0.13	0.12	0.12	0.11	0.13
LOI	0.54	0.99	0.36	0.31	0.43	0.55	0.54	0.48	0.49	0.50	0.95
Total	99.61	99.52	99.55	99.62	99.55	99.74	100.15	99.70	99.51	99.53	99.54
$Mg^{\#}$	36	37	28	27	35	35	35	34	34	34	36
Na_2O/K_2O	0.92	1.04	0.94	0.78	0.83	0.95	0.96	0.78	0.78	0.67	1.37
A/CNK	0.98	0.93	1.01	1.03	1.04	1.05	1.00	1.04	1.04	1.04	0.85
σ	2.11	1.81	1.48	1.46	2.09	2.38	2.28	2.55	2.54	3.19	2.61
Ba	407	341	293	267	505	1481	1511	1488	1501	1650	967
Rb	177	153	136	151	166	88	88	99	100	107	86
Cs	6.51	5.56	4.11	4.36	8.69	4.52	4.32	3.25	3.31	3.01	3.82
Th	15.19	16.24	17.23	7.53	12.26	13.44	16.85	15.15	13.08	15.62	16.90
U	4.96	3.91	7.51	4.08	2.84	1.18	1.14	1.53	1.42	1.31	1.37
Nb	11.94	11.67	7.98	8.11	9.97	5.91	5.66	6.20	6.24	5.79	6.59
Ta	1.86	1.67	1.06	1.28	1.20	0.31	0.29	0.36	0.37	0.32	0.38
K	34285	29968	30633	33372	35780	33870	33870	38602	38436	45243	29221
Pb	27.80	25.46	27.02	27.61	27.12	20.19	20.58	20.95	21.08	25.52	17.19
Sr	186	177	112	108	206	364	348	333	336	347	309
Zr	80	134	75	74	141	296	263	308	346	284	328
Hf	2.99	3.89	2.54	2.50	3.98	6.36	5.66	6.69	7.54	6.26	7.33

(*Continued*)

No. Rocks	AYQ-9 monzonitic granite	AYQ-10 monzonitic granite	AYQ-11 monzonitic granite	AYQ-12 monzonitic granite	AYQ-13 monzonitic granite	AYQ-17 biotite granite	AYQ-18 biotite granite	AYQ-19 biotite granite	AYQ-19R biotite granite	AYQ-20 biotite granite	AYQ-21 biotite granite
P	393	349	175	175	349	567	567	524	524	480	567
Ti	1498	1558	719	719	1498	2517	2278	2397	2397	2098	2637
Y	28.20	25.80	54.37	31.62	21.86	8.62	8.38	11.86	11.84	10.45	11.61
Cr	9.49	7.04	1.85	2.92	5.87	5.30	5.66	4.58	4.81	36.67	9.62
Ni	2.65	3.60	1.11	1.71	2.61	2.67	2.91	2.28	2.36	18.84	6.26
La	24.69	24.98	13.83	8.36	24.23	67.39	81.71	86.09	79.83	87.61	90.71
Ce	51.94	51.85	29.95	17.28	51.63	121.72	145.71	155.49	143.57	157.63	164.04
Pr	5.86	5.74	3.46	2.05	5.51	11.68	13.92	15.03	13.75	14.99	15.64
Nd	21.64	21.17	13.45	7.98	20.19	37.02	43.44	47.36	43.70	47.29	50.27
Sm	4.47	4.25	3.47	2.17	3.88	4.37	4.87	5.69	5.24	5.45	6.05
Eu	0.69	0.66	0.54	0.50	0.77	1.43	1.40	1.41	1.42	1.46	1.26
Gd	4.52	4.21	5.24	3.21	3.73	2.81	2.98	3.76	3.52	3.44	3.86
Tb	0.68	0.63	0.97	0.59	0.55	0.34	0.35	0.46	0.43	0.41	0.46
Dy	4.32	3.92	7.28	4.30	3.38	1.68	1.67	2.28	2.23	2.01	2.28
Ho	0.90	0.81	1.73	0.98	0.70	0.30	0.29	0.40	0.41	0.36	0.40
Er	2.71	2.46	5.35	3.04	2.09	0.86	0.81	1.18	1.19	1.06	1.16
Tm	0.44	0.40	0.84	0.50	0.34	0.13	0.12	0.17	0.17	0.15	0.16
Yb	3.05	2.75	5.44	3.43	2.29	1.17	0.97	1.13	1.17	1.03	1.10
Lu	0.46	0.42	0.80	0.51	0.35	0.20	0.17	0.18	0.19	0.17	0.18
∑REE	126.4	124.25	92.35	54.90	119.64	251.1	298.41	320.63	296.82	323.06	337.57
Sr/Y	6.58	6.86	2.06	3.40	9.42	42.20	41.58	28.05	28.33	33.23	26.66
La/Yb	8.08	9.07	2.54	2.44	10.59	57.62	83.96	76.23	67.94	84.97	82.23
$(La/Yb)_N$	5.80	6.51	1.82	1.75	7.59	41.33	60.23	54.68	48.73	60.95	58.98
Y/Yb	9.24	9.37	9.99	9.23	9.55	7.37	8.61	10.50	10.08	10.13	10.52
Eu/Eu*	0.47	0.47	0.39	0.58	0.61	1.17	1.04	0.87	0.95	0.96	0.74
La/Ce	0.48	0.48	0.46	0.48	0.47	0.55	0.56	0.55	0.56	0.56	0.55
Rb/Sr	0.95	0.87	1.21	1.40	0.81	0.24	0.25	0.30	0.30	0.31	0.28
$(Gd/Yb)_N$	1.22	1.26	0.80	0.77	1.35	1.99	2.54	2.76	2.48	2.76	2.89

Note: Major elements were analyzed by XRF (in wt. %) and trace elements were analyzed by ICP-MS (in ppm). Test unit: The major elements were analyzed by the State Key Laboratory of Continental Dynamics, Northwest University; trace elements in quartz diorite, tonalite, and biotite granite were analyzed by the State Key Laboratory of Continental Dynamics, Northwest University; and those in monzogranite were completed by the Institute of Geochemistry in Guangzhou. $Eu/Eu^* = Eu_N/(Eu_N \times Gd_N)^{1/2}$; $\sigma = ((K_2O + Na_2O) \times (K_2O + Na_2O))/(SiO_2 - 43)$.

The aluminum saturation index (ACNK) values range from 0.91 to 0.96, and the samples plot in the metaluminous field of the aluminum saturation index diagram (Fig. 8).

In primitive mantle-normalized trace element spider diagrams (Fig. 9(a)), the samples display enrichment in Rb, Ba, Th, U, and Sr, but depletion in Nb, Ta, Ti, and HREE with positive Sr anomalies. In the chondrite-normalized rare earth element (REE) diagrams (Fig. 9(b)), they exhibit moderate LREE enrichment, $(La/Yb)_N$ = 5.22–10.86, and slightly positive Eu anomalies (δEu = 0.97–1.18). The HREEs show flat patterns. In addition, the samples exhibit relatively high Sr (582–620 ppm (parts per million)) and Sr/Y (35.11–53.18), Y/Yb (10.98–11.21), and La/Yb (7.28–15.14) ratios, but low Y (11.41–16.72 ppm), Yb (1.02–1.51 ppm), Ni (10.33–11.55 ppm), Cr (13.35–16.84 ppm), Rb/Sr (0.03–0.05) and La/Ce (0.42–0.50).

5.2.2 Tonalite (~246.5 Ma)

The tonalites have SiO_2 contents ranging from 62.14 wt% to 68.94 wt% (Table 1) and an average Al_2O_3 content of 16.50 wt%. They exhibit relatively high Na_2O (Na_2O/K_2O = 1.72), CaO (average 3.39 wt%), and $^TFe_2O_3$ (average 3.76 wt%). The MgO contents of the samples have an average of 1.49%, and the Mg-number ($Mg^{\#}$) values vary from 41 to 47. The sample points plot in the calc-alkaline series of the SiO_2-K_2O diagram (Fig. 7(a)) and in the granodiorite field of the SiO_2-($Na_2O + K_2O$) discrimina-

Table 2 Zircon LA-ICP-MS U-Pb ages of rocks

Sample number	Pb	Th	U	Th/U	Isotope ratio						Surface age			
Analysis point number	$\times10^{-6}$				$^{207}Pb/^{206}Pb$	±%	$^{207}Pb/^{235}U$	±%	$^{206}Pb/^{238}U$	±%	$^{207}Pb/^{235}U$	1σ	$^{206}Pb/^{238}U$	1σ
The quartz diorite (TW-4)														
TW4-05	19.65	60.80	80.70	0.75	0.0528	0.0024	0.3408	0.0125	0.0468	0.0008	298	9	295	5
TW4-06	21.83	76.61	86.69	0.88	0.0524	0.0034	0.3386	0.0196	0.0469	0.0009	296	15	296	6
TW4-07	15.83	46.64	62.13	0.75	0.0521	0.0028	0.3469	0.0162	0.0483	0.0009	302	12	304	5
TW4-09	13.06	34.95	53.17	0.66	0.0535	0.0054	0.3510	0.0336	0.0476	0.0013	305	25	300	8
TW4-13	10.34	31.25	44.14	0.71	0.0529	0.0052	0.3523	0.0326	0.0483	0.0013	306	24	304	8
TW4-15	16.22	44.34	70.10	0.63	0.0532	0.0052	0.3576	0.0331	0.0487	0.0013	310	25	307	8
TW4-16	8.11	17.69	31.89	0.55	0.0522	0.0039	0.3502	0.0239	0.0487	0.0010	305	18	307	6
TW4-22	13.65	34.20	61.32	0.56	0.0517	0.0040	0.3460	0.0245	0.0486	0.0011	302	18	306	7
TW4-23	15.25	44.66	67.23	0.66	0.0498	0.0033	0.3351	0.0202	0.0488	0.0010	294	15	307	6
TW4-24	26.58	79.38	118.13	0.67	0.0528	0.0071	0.3493	0.0451	0.0480	0.0017	304	34	302	10
TW4-25	14.27	45.73	69.54	0.66	0.0526	0.0046	0.3447	0.0283	0.0476	0.0012	301	21	300	7
TW4-26	11.74	24.86	49.02	0.51	0.0525	0.0054	0.3494	0.0341	0.0483	0.0013	304	26	304	8
TW4-27	10.29	26.98	40.58	0.66	0.0531	0.0060	0.3492	0.0375	0.0477	0.0014	304	28	300	9
TW4-30	13.27	32.74	61.24	0.53	0.0522	0.0031	0.3484	0.0184	0.0484	0.0009	304	14	305	6
TW4-31	10.31	23.46	38.24	0.61	0.0515	0.0105	0.3460	0.0684	0.0487	0.0024	302	52	307	14
TW4-32	12.43	38.38	57.97	0.66	0.0535	0.0050	0.3494	0.0308	0.0474	0.0012	304	23	298	7
TW4-33	14.94	34.57	70.47	0.49	0.0528	0.0032	0.3480	0.0187	0.0479	0.0009	303	14	301	6
TW4-34	14.20	36.88	61.42	0.60	0.0530	0.0054	0.3511	0.0337	0.0481	0.0013	306	25	303	8
TW4-35	10.97	29.46	50.92	0.58	0.0517	0.0042	0.3451	0.0259	0.0485	0.0011	301	20	305	7

Table 2 (continued)

Sample number	Pb	Th	U	Th/U	Isotope ratio						Surface age			
Analysis point number	$\times10^{-6}$				$^{207}Pb/^{206}Pb$	±%	$^{207}Pb/^{235}U$	±%	$^{206}Pb/^{238}U$	±%	$^{207}Pb/^{235}U$	1σ	$^{206}Pb/^{238}U$	1σ
The tonalite (TW-6)														
TW6-05	156.41	429.37	818.57	0.52	0.0568	0.0022	0.3011	0.0078	0.0385	0.0006	267	6	243	3
TW6-06	104.55	192.00	559.01	0.34	0.0567	0.0049	0.3012	0.0240	0.0385	0.0009	267	19	244	6
TW6-07	137.76	512.39	705.82	0.73	0.0570	0.0031	0.3006	0.0141	0.0383	0.0007	267	11	242	4
TW6-09	57.96	152.27	304.04	0.50	0.0515	0.0032	0.2784	0.0152	0.0392	0.0007	249	12	248	4
TW6-13	210.61	385.99	1118.63	0.35	0.0553	0.0019	0.2945	0.0061	0.0387	0.0005	262	5	245	3
TW6-15	44.10	137.15	215.44	0.64	0.0545	0.0075	0.2922	0.0387	0.0389	0.0014	260	30	246	8
TW6-16	213.66	458.69	1106.96	0.41	0.0524	0.0019	0.2841	0.0065	0.0394	0.0006	254	5	249	3
TW6-17	70.11	261.42	344.18	0.76	0.0513	0.0021	0.2779	0.0086	0.0393	0.0006	249	7	248	4
TW6-18	72.61	309.84	352.83	0.88	0.0518	0.0022	0.2818	0.0094	0.0394	0.0006	252	7	249	4
TW6-22	67.64	199.55	331.94	0.60	0.0526	0.0027	0.2879	0.0121	0.0397	0.0007	257	10	251	4
TW6-23	81.44	227.95	409.04	0.56	0.0537	0.0018	0.2918	0.0060	0.0394	0.0006	260	5	249	3
TW6-25	108.12	357.91	553.15	0.65	0.0532	0.0047	0.2826	0.0234	0.0386	0.0009	253	19	244	6
TW6-26	54.43	169.98	270.85	0.63	0.0517	0.0025	0.2789	0.0109	0.0391	0.0006	250	9	247	4
TW6-27	109.12	346.75	550.70	0.63	0.0551	0.0026	0.2926	0.0110	0.0386	0.0006	261	9	244	4
TW6-31	54.77	136.42	272.42	0.50	0.0526	0.0027	0.2889	0.0121	0.0399	0.0007	258	10	252	4
TW6-32	136.68	318.22	684.10	0.47	0.0527	0.0027	0.2896	0.0126	0.0398	0.0007	258	10	252	4
TW6-34	168.75	456.91	850.56	0.54	0.0565	0.0035	0.2996	0.0164	0.0385	0.0007	266	13	244	5
TW6-35	157.76	371.01	806.26	0.46	0.0559	0.0024	0.2924	0.0094	0.0379	0.0006	260	7	240	4

Table 2 (continued)

Sample number	Pb	Th	U	Th/U	Isotope ratio						Surface age			
Analysis point number	$\times10^{-6}$				$^{207}Pb/^{206}Pb$	±%	$^{207}Pb/^{235}U$	±%	$^{206}Pb/^{238}U$	±%	$^{207}Pb/^{235}U$	1σ	$^{206}Pb/^{238}U$	1σ
The monzonitic granite (TW-2)														
TW2-05	141.34	349.49	747.33	0.47	0.0558	0.0035	0.2855	0.0160	0.0371	0.0007	255	13	235	5
TW2-07	763.54	1440.00	4187.52	0.34	0.0562	0.0025	0.2817	0.0102	0.0363	0.0006	252	8	230	4
TW2-08	100.32	196.79	522.26	0.38	0.0055	0.0020	0.2862	0.0074	0.0378	0.0006	256	6	239	4
TW2-10	87.81	178.19	464.72	0.38	0.0558	0.0024	0.2843	0.0098	0.0370	0.0006	254	8	234	4
TW2-13	390.48	464.87	2091.35	0.22	0.0539	0.0021	0.2803	0.0080	0.0378	0.0006	251	6	239	4
TW2-14	124.08	252.48	658.44	0.38	0.0537	0.0018	0.2739	0.0055	0.0370	0.0005	246	4	234	3
TW2-18	761.82	644.41	4070.38	0.16	0.0568	0.0018	0.2939	0.0057	0.0376	0.0005	262	5	238	3
TW2-23	779.77	756.33	4166.91	0.18	0.0551	0.0028	0.2786	0.0119	0.0367	0.0006	250	9	232	4
TW2-26	118.38	354.82	593.46	0.60	0.0542	0.0019	0.2790	0.0061	0.0374	0.0005	250	5	237	3
TW2-27	155.70	309.42	786.08	0.39	0.0609	0.0048	0.3079	0.0221	0.0367	0.0009	273	17	232	5
TW2-30	105.48	118.53	555.40	0.21	0.0566	0.0031	0.2862	0.0137	0.0367	0.0007	256	11	232	4
TW2-31	55.36	138.53	274.79	0.50	0.0556	0.0034	0.2851	0.0152	0.0372	0.0007	255	12	236	4
TW2-32	117.23	263.91	598.71	0.44	0.0505	0.0020	0.2629	0.0074	0.0377	0.0006	237	6	239	4
TW2-34	83.29	173.62	423.40	0.41	0.0531	0.0020	0.2724	0.0070	0.0372	0.0006	245	6	236	3
TW2-35	141.50	546.96	686.60	0.80	0.0575	0.0020	0.2887	0.0068	0.0364	0.0005	258	5	231	3

Table 2 (continued)

Sample number	Pb	Th	U	Th/U	Isotope ratio						Surface age			
Analysis point number	$\times10^{-6}$				$^{207}Pb/^{206}Pb$	±%	$^{207}Pb/^{235}U$	±%	$^{206}Pb/^{238}U$	±%	$^{207}Pb/^{235}U$	1σ	$^{206}Pb/^{238}U$	1σ
The biotite granite (TW-3)														
TW3-05	41.53	191.15	216.93	0.88	0.0592	0.0067	0.2935	0.0313	0.0360	0.0011	261	25	228	7
TW3-06	15.48	89.49	74.57	1.20	0.0592	0.0086	0.2942	0.0410	0.0361	0.0013	262	32	228	8
TW3-07	39.21	264.30	204.69	1.29	0.0546	0.0055	0.2728	0.0258	0.0363	0.0010	245	21	230	6
TW3-08	22.60	133.51	115.03	1.16	0.0518	0.0083	0.2567	0.0399	0.0359	0.0014	232	32	228	9
TW3-09	34.67	157.37	191.80	0.82	0.0555	0.0046	0.2775	0.0215	0.0363	0.0009	249	17	230	5
TW3-10	22.51	142.52	119.05	1.20	0.0544	0.0034	0.2720	0.0151	0.0363	0.0007	244	12	230	4
TW3-14	38.40	223.65	190.66	1.17	0.0559	0.0076	0.2767	0.0362	0.0359	0.0013	248	29	228	8
TW3-16	93.23	283.62	539.08	0.53	0.0555	0.0027	0.2770	0.0109	0.0362	0.0006	248	9	229	4
TW3-17	35.29	259.60	187.50	1.39	0.0575	0.0056	0.2803	0.0257	0.0354	0.0010	251	20	224	6
TW3-18	32.15	172.05	163.71	1.05	0.0531	0.0040	0.2678	0.0185	0.0366	0.0008	241	15	232	5
TW3-23	38.29	192.77	209.41	0.92	0.0551	0.0025	0.2742	0.0099	0.0361	0.0006	246	8	229	4
TW3-24	53.03	246.71	294.25	0.84	0.0574	0.0053	0.2887	0.0250	0.0365	0.0009	258	20	231	6
TW3-25	33.31	179.65	184.52	0.97	0.0560	0.0072	0.2808	0.0345	0.0364	0.0012	251	27	230	8
TW3-27	22.23	146.19	116.34	1.26	0.0558	0.0052	0.2785	0.0243	0.0362	0.0009	249	19	229	6
TW3-30	31.30	229.49	158.60	1.45	0.0514	0.0035	0.2575	0.0157	0.0363	0.0007	233	13	230	5
TW3-33	32.66	185.63	182.80	1.02	0.0460	0.0027	0.2316	0.0122	0.0365	0.0006	212	10	231	4
TW3-34	22.94	135.03	127.77	1.06	0.0510	0.0039	0.2572	0.0180	0.0366	0.0008	232	15	232	5
TW3-35	23.28	153.44	130.55	1.18	0.0562	0.0055	0.2778	0.0258	0.0359	0.0010	249	20	227	6

Notes: Errors are 1σ. Common Pb was corrected using measured ^{204}Pb. Testing: State Key Laboratory of Continental Dynamics, Northwest University

tion diagram (Fig. 7(b)). The ACNK values range from 0.95 to 1.13, and the samples plot in the metaluminous and slightly peraluminous I-type fields on the aluminum saturation index diagram (Fig. 8).

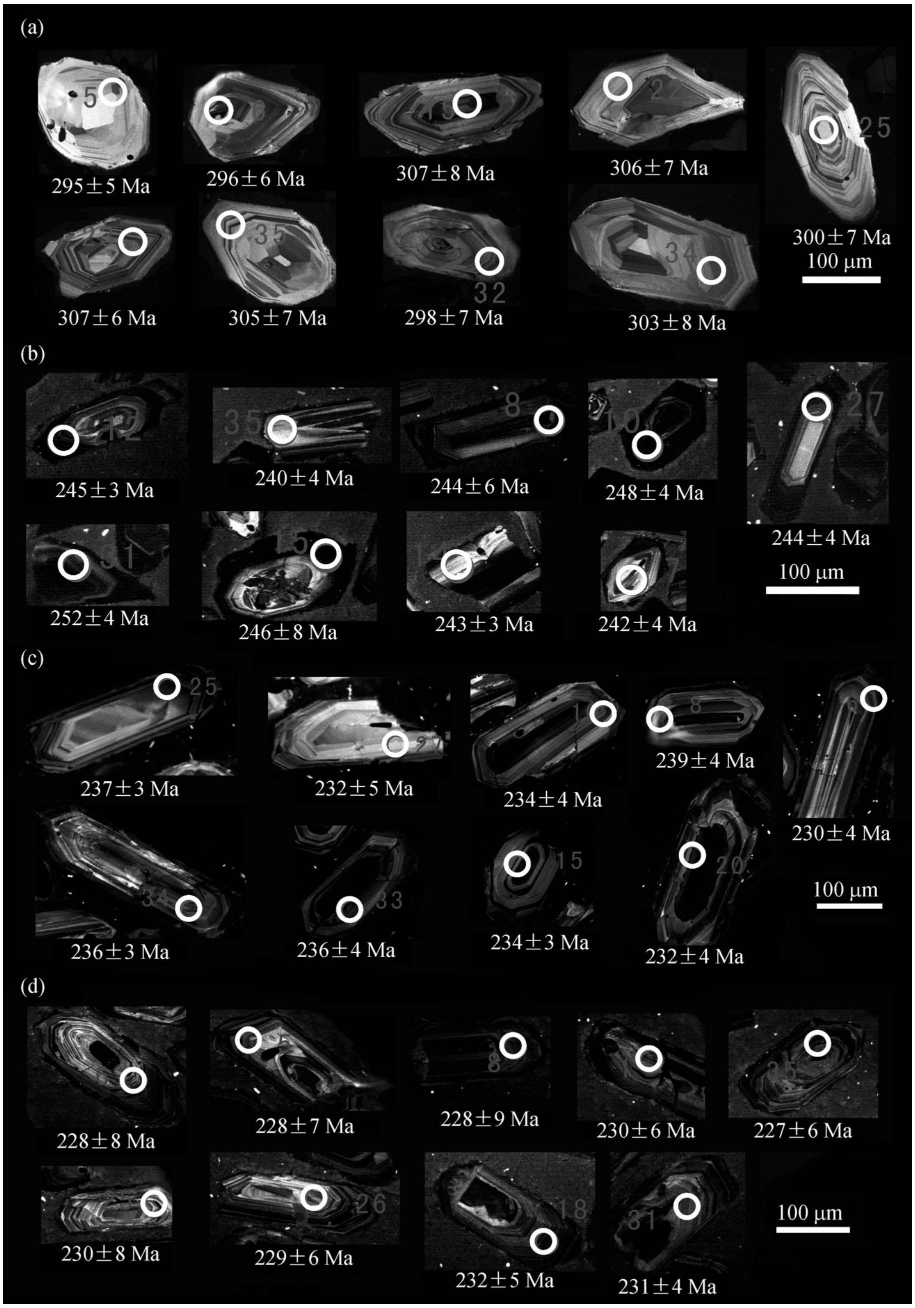

Fig. 5 Cathodoluminescence (CL) images of selected zircons. (a) Quartz diorite; (b) tonalite; (c) monzogranite; (d) biotite granite.

In the primitive mantle-normalized trace element spider diagrams (Fig. 9(c)), the samples display enrichment in Rb, Ba, Th, and K and depletion in Nb, Ta, P, and Ti. In the chondrite-normalized rare earth element diagrams (Fig. 9(d)), there are extreme differentiations between the LREEs and HREEs and moderately negative Eu anomalies (δEu = 0.75–0.80). In addition, the samples exhibit relatively high abundances of Sr (average of 371.28 ppm), Y (average of 29.68 ppm), and Yb (average of 2.47 ppm), and high Rb/Sr ratios (0.24–0.34), but low La/Ce (0.47–0.52) ratios.

5.2.3 Monzogranite (~235 Ma)

The monzogranites have SiO_2 contents ranging from 72.72 to 78.13 wt% (Table 1) and Al_2O_3 contents ranging from 11.56 wt% to 14.07 wt%. They exhibit relatively equivalent Na_2O (3.15–3.80 wt%) and K_2O (3.61–4.31 wt%, K_2O/Na_2O = 0.97–1.28) values, but low CaO (0.93–2.32 wt%), MgO (0.20–0.56 wt%, $Mg^{\#}$ = 27–37), and TiO_2 (0.12–0.26 wt%). The sample points plot in the high-K calc-alkaline series of the SiO_2-K_2O diagram (Fig. 7(a))

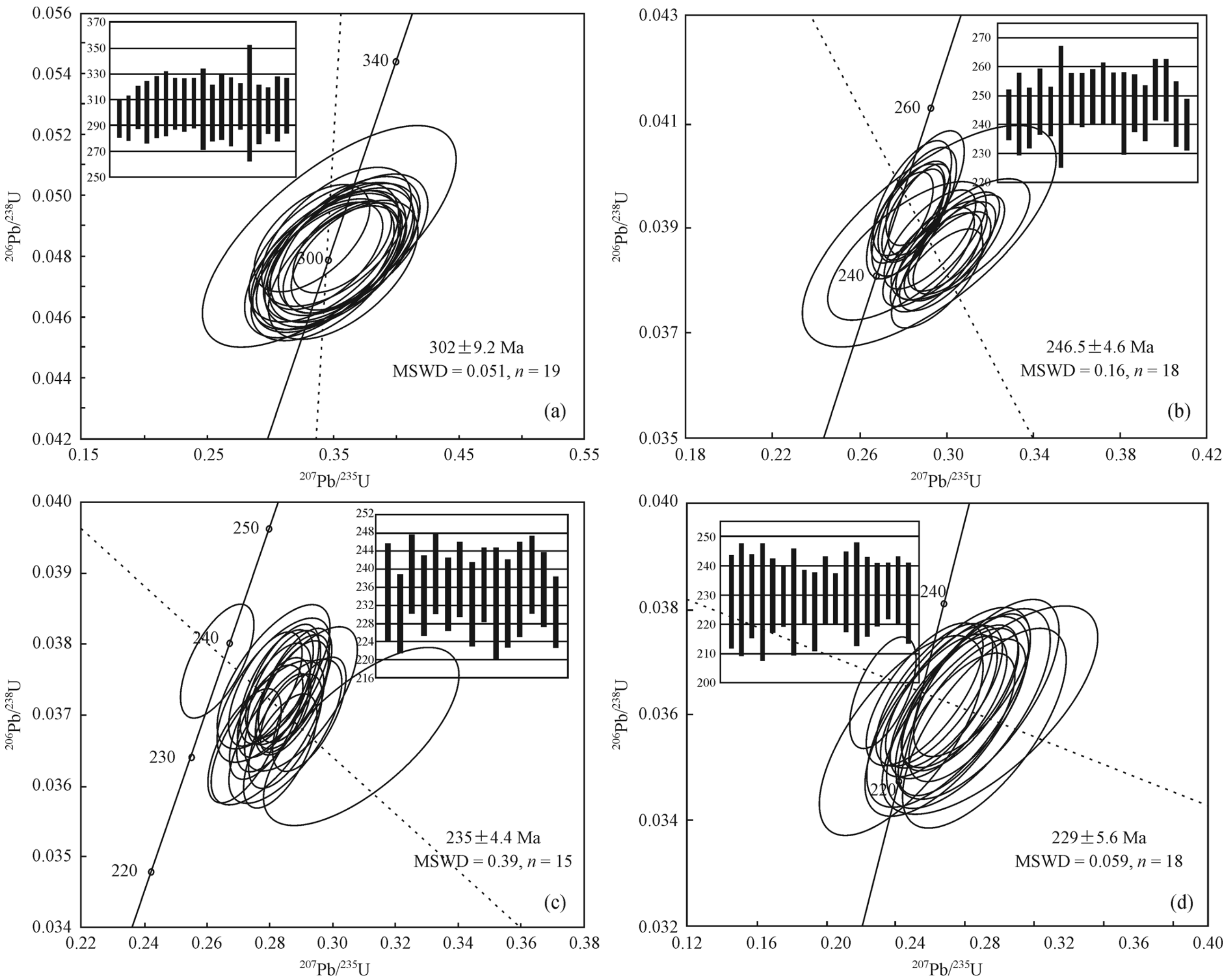

Fig. 6 Zircon U-Pb isotopic concordia diagram and relative probability diagrams. (a) Quartz diorite; (b) tonalite; (c) monzogranite; (d) biotite granite.

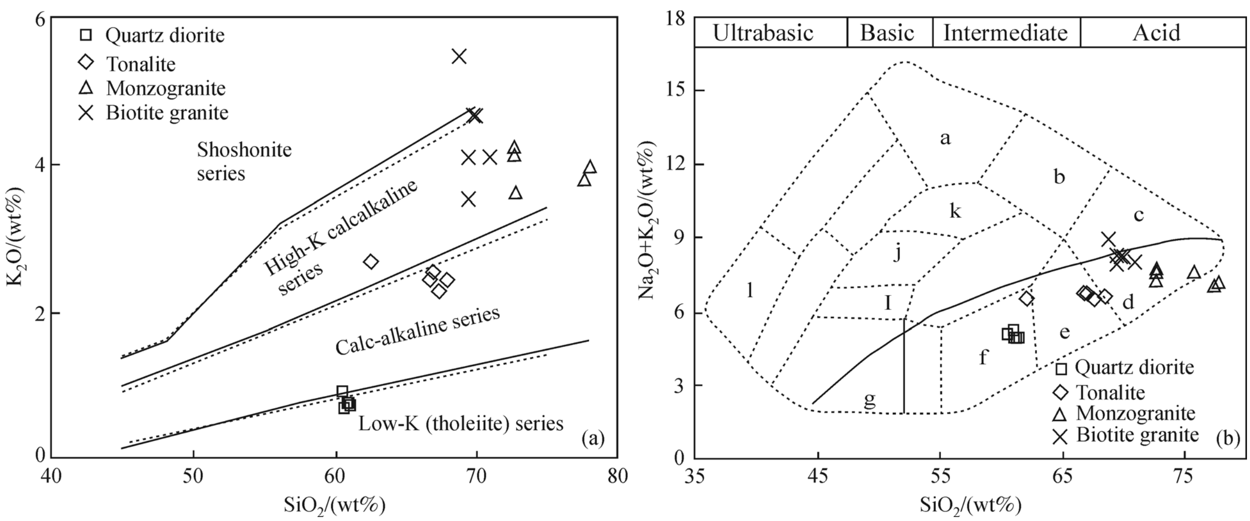

Fig. 7 Granite SiO_2-K_2O discrimination diagram (a) (the solid line is after Peccerillo and Taylor, 1976, and the broken line is after Middlemost, 1985) and SiO_2-($K_2O + Na_2O$) classification diagram of granite (b) (Wilson, 1989). a-nepheline syenite; b-syenite; c-alkaline granites; d-granite; e-quartz diorite, granodiorite; f-diorite; g-gabbro; h-gabbro; I-gabbro; j-syenite diorite; k-syenite; l-iolite (the solid line distinguishes alkaline from sub-alkaline rocks).

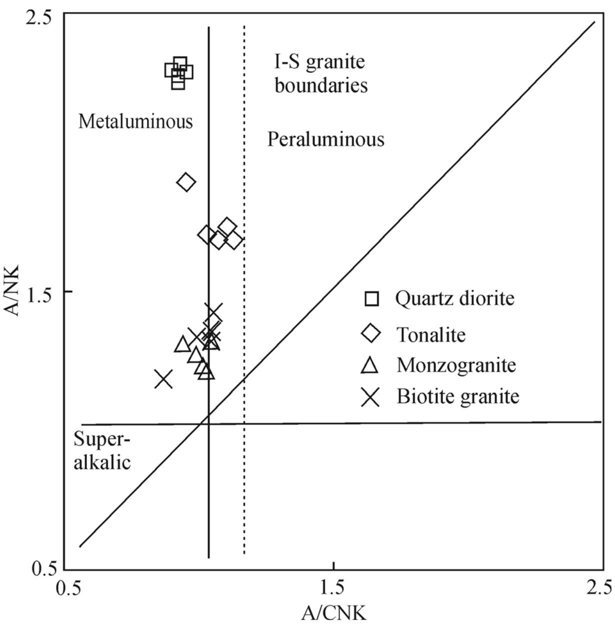

Fig. 8 A/NK-A/CNK discriminant diagram (after Maniar and Piccoli, 1989).

and in the granite field of the SiO_2-($Na_2O + K_2O$) discrimination diagram (Fig. 7(b)). The ACNK values range from 0.93 to 1.04, and the samples plot in the quasi-aluminous field of the aluminum saturation index diagram (Fig. 8).

In the primitive-mantle-normalized trace element spider diagrams (Fig. 9(e)), the samples display enrichment in Th and K, but strong depletion in Nb, Ta, Sr, P, and Ti. In the chondrite-normalized rare earth element diagrams (Fig. 9 (f)), they exhibit LREE enrichment [$(La/Yb)_N$ = 1.75–7.59], extreme differentiation between LREEs and HREEs, and strong negative Eu anomalies (δEu = 0.39–0.61). In addition, they exhibit relatively high Rb/Sr (0.81–1.40) but low La/Ce (0.46–0.48) ratios.

5.2.4 Biotite granite (~229.5 Ma)

The biotite granites have SiO_2 contents ranging from 68.89 to 71.04 wt% (Table 1) and Al_2O_3 contents ranging from 13.95 wt% to 15.76 wt%. They exhibit high CaO (1.75–2.54 wt%), relatively equivalent Na_2O (3.63–4.81 wt%) and K_2O (3.52–5.45 wt%, Na_2O/K_2O = 0.67–1.37), and low MgO (0.63–0.81 wt%) and TiO_2 (0.35–0.44 wt%), with low $Mg^{\#}$ (34–36). The sample points plot in the high-K calc-alkaline series of the SiO_2-K_2O diagram (Fig. 7(a)) and in the granite field of the SiO_2-($Na_2O + K_2O$) discrimination diagrams (Fig. 7(b)). The ACNK values range from 0.85 to 1.05, and the samples plot in the metaluminous field of the aluminum saturation index diagram (Fig. 8).

In the primitive-mantle-normalized trace element spider diagrams (Fig. 9(g)), the samples display enrichment in Ba, Rb, and Th, but strong depletion in Nb, Ta, Sr, P, and Ti. In the chondrite-normalized rare earth element diagrams (Fig. 9(h)), they exhibit LREE enrichment [$(La/Yb)_N$ = 41.33–60.95], extreme differentiation between LREEs and HREEs, and a lack of notably negative Eu anomalies (δEu = 0.74–1.17).

6 Discussion

6.1 Petrogenesis

6.1.1 Quartz diorite (~302 Ma)

All the quartz diorites share the geochemical affinities of adakites such as high Al_2O_3, Sr, Sr/Y ratio, and depletion in low Y and Yb contents (Defant et al., 1991; Drummond et al., 1996; Martin, 1999; Zhang et al., 2010). The REE data defined listric-shaped REE profiles on chondrite-normalized diagrams, implying the fractionation of amphibole (Richards and Kerrich, 2007). As we all know, the removal of amphibole would produce a decrease in Dy/Yb ratio. However, the negative correlation between Dy/Yb and SiO_2 is not observed in a Harker diagram (not shown).

In the SiO_2-MgO diagram (Fig. 10), all the quartz diorites plot within the adakite field. There are several genetic models proposed to interpret the origin of adakitic rocks: 1) partial melting of a young, hot subducted slab (e.g., Drummond and Defant, 1990); 2) crustal assimilation and fractional crystallization (AFC) of basaltic magmas at high pressure conditions (e.g., Castillo et al., 1999; Macpherson et al., 2006); and 3) partial melting of a thickened lower crust (e.g., Muir et al., 1995).

In general, those adakitic rocks derived from AFC of basaltic magmas are a component of a suite of igneous rocks with basaltic-andesitic-rhyolitic compositions (Castillo et al., 1999). But basaltic and rhyolitic rocks are not observed near these quartz diorites. Additionally, the absence of inherited zircons and relatively high Mg# (48–51) implied that they did not likely originate from fractional crystallization of primary basaltic magmas with old crustal contaminant (Castillo et al., 1999).

Thickened lower crust-derived adakitic rocks are enriched in K_2O content but depleted in Na_2O content in contrast with our samples. Recently, Hou et al. (2004) suggested that the Gangdese adakitic intrusions originating from the lower crust exhibit high Rb/Sr ratios (> 0.05). In contrast, our quartz diorites have relatively low Rb/Sr ratios (0.032–0.046). More importantly, those adakitic rocks are generally exposed in some specific regions which have undergone crustal thickening, e.g. orogenic belts (Kay et al., 1993; Wang et al., 2006). The quartz diorites (adakites) with high Al and Na_2O contents argue against

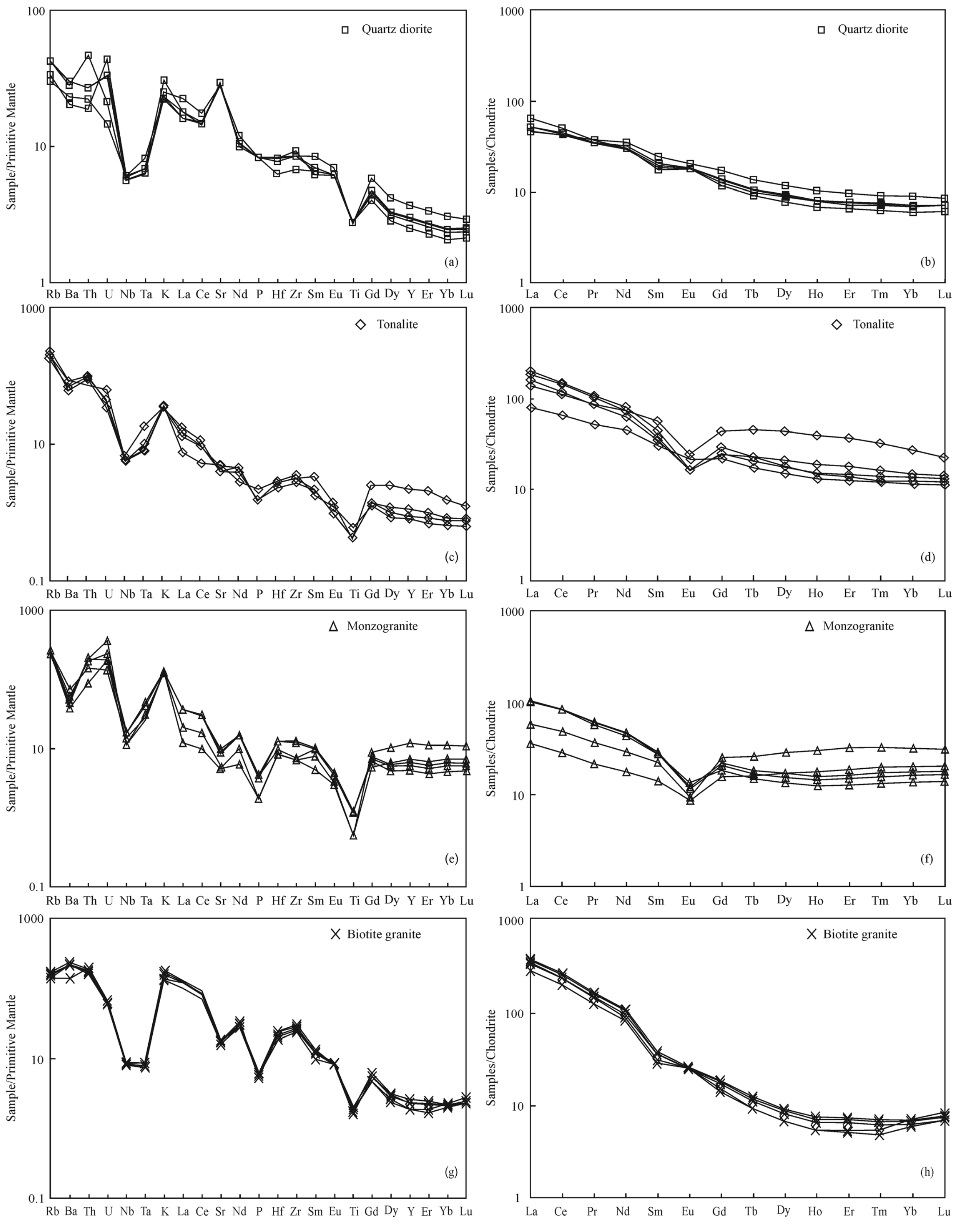

Fig. 9 PM-normalized trace element spider diagrams and chondrite-normalized REE patterns for the quartz diorite (a) (b), tonalite (c) (d), monzogranite (e) (f), biotite granite (g) (h) (PM-normalized values and chondrite-normalized values from Sun and McDonough, 1989).

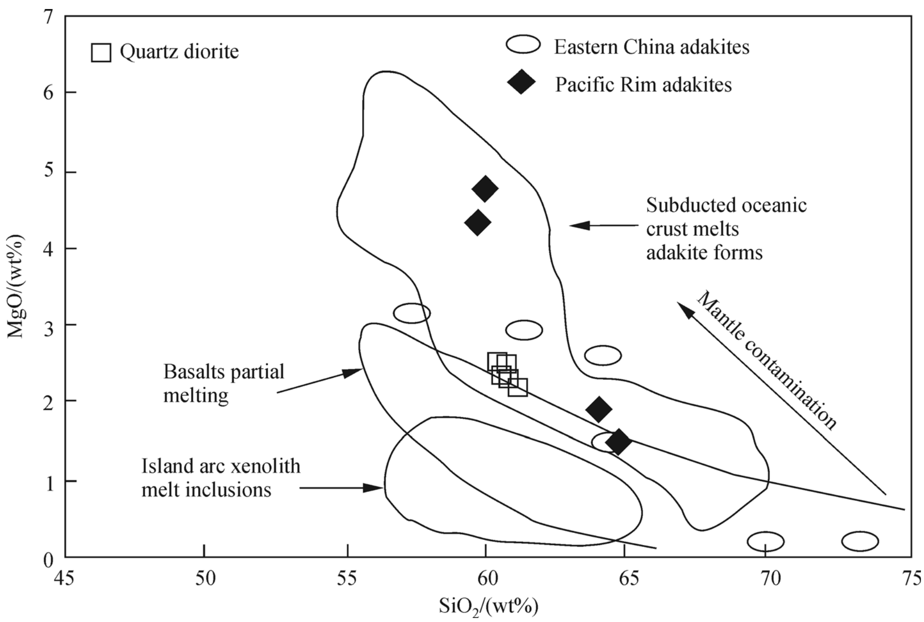

Fig. 10 Quartz diorite and tonalite SiO_2-MgO diagram (Rapp, 1997; adakite in eastern China and the Pacific quoted from Zhang et al., 2001b).

the model that they were not partial melts of lower continental crust which are characterized by high K_2O and ($Na_2O + K_2O$) contents and low Al_2O_3 contents (Atherton and Petford, 1993; Kay et al., 1993; Drummond et al., 1996; Kay and Mpodozis, 2001; Zhang et al., 2001a, b, c, 2002a; Mao et al., 2012). As we will discuss below, there was no crustal thickening process before the emplacement of these quartz diorites. Consequently, it was difficult to envisage that they were produced by partial melting of a thickened lower crust.

An alternative genetic model was that these quartz diorites were likely derived by partial melting of a subducted oceanic slab. This viewpoint was supported by their high Na_2O, Na_2O/K_2O, and low K_2O varying from 0.67–0.92 wt% (Martin, 1999). Previous studies indicated that slab-derived adakitic melts show relatively low Rb/Sr ratios with a range from 0.01 to 0.04 (Drummond et al., 1996). The low Rb/Sr ratios in our samples further supported a subducted slab as their source. The relatively high Mg-number ($Mg^{\#}$ = 48–51) is attributed to gradual assimilation of slab melts by asthenospheric mantle during ascent. All these features suggested that the quartz diorites were derived from a subducted oceanic slab (Sen and Dunn, 1994; Martin, 1999; Rapp et al., 1999; Xu and Ma, 2003; Wang et al., 2007b; Mao et al., 2012). The $(La/Yb)_N$-Yb_N and Sr/Y-Y diagrams (Fig. 11) showed that the protolith is roughly a garnet amphibolite, which indicates that the source region might not have residual plagioclases, but rather amphiboles, garnets, and Fe-Ti oxides (ilmenites, rutiles, etc.).

6.1.2 Tonalite (~246.5 Ma)

All the tonalites are also calc-alkaline series and share geochemical affinities of I-type granites. They are characterized by high SiO_2, Al_2O_3, and Na_2O, low K_2O, moderate negative Eu anomaly and negative Nb, Ta, Ti anomalies. The occurrence of amphibole in Fig. 4(b) further suggested that they are I-type granites.

The relative high $Mg^{\#}$ (41–47) suggested that these felsic rocks were likely produced by fractional crystallization of mantle-derived basaltic magmas. The speculation was supported by negative correlations between MgO, ${}^{T}Fe_2O_3$, $Mg^{\#}$, compatible elements (e.g., Cr and Ni) and SiO_2. These correlations might be attributed to the removal of mafic minerals including biotite and amphibole, inferred by the occurrence of these minerals in Fig. 4(c). The negative Nb-Ta-Ti anomalies in these tonalites suggested that the lithospheric mantle source had been modified by subducted slab-released components. Consequently, we considered that the tonalites were likely derived by fractional crystallization of a modified lithospheric mantle-derived basaltic magma.

6.1.3 Monzogranite (~235 Ma)

All the monzogranites are characterized by high SiO_2 and K_2O, low Al_2O_3, CaO, ${}^{T}Fe_2O_3$, MgO, and TiO_2, and display metaluminous and high-K calc-alkaline signatures. They exhibit geochemical characteristics of mafic rocks-derived from partial melts in continental crust (Li et al.,

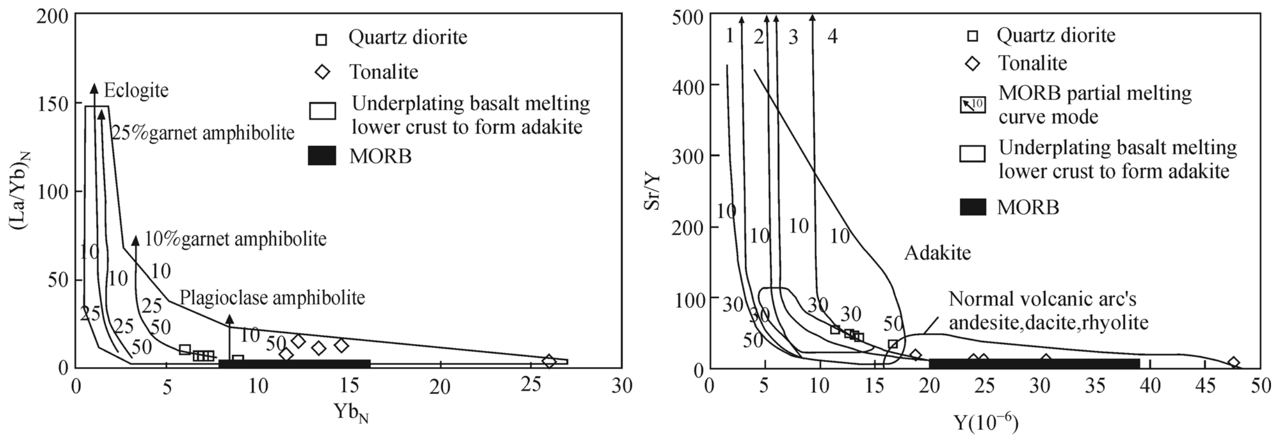

Fig. 11 $(La/Yb)_N$-Yb_N and Sr/Y-Y diagrams of the quartz diorite and tonalite. (Chappell and White, 1974; Drummond and Defant, 1990). Sr/Y-Y diagram: 1. eclogite (garnet/pyroxene = 50/50); 2. amphibole garnet (garnet/amphibole = 50/50); 3. amphibole eclogite (amphibole/garnet/pyroxene = 10/40/50); 4. garnet amphibolite (garnet/amphibole = 10/90).

2007). In the Ga/Al diagram (Fig. 12), the samples are plotted within the I-S field. Additionally, standard CIPW calculations show that the rocks contain diopside, but < 1 wt% corundum (not shown in table), indicating that the monzogranites are I-type granites.

According to the trace element geochemistry, all the monzogranites display enrichment in Rb, Th, and K, but strong depletion in Ba, Nb, Ta, Sr, P, and Ti. Low P and Ti may be associated with the fractional crystallization of ilmenite, sphene, and apatite. The depletion of Nb and Ta may be associated with the depletion of crustal magma, and the high Rb/Sr ratio indicates that the magma source is a crustal source (Rubatto and Hermann, 2003). The coeval basaltic magmas were required for triggering partial melting of the crustal source.

6.1.4 Biotite granite (~229.5 Ma)

The biotite granites are characterized by high SiO_2 and Al_2O_3 contents, and low Mg and TiO_2 contents with ASI < 1.1. A CIPW standard mineralogy calculation shows corundum < 1 wt% (no table). All the evidence indicate that the biotite granites belong to I-type granites (Fig. 12).

All the samples display enrichment of Ba, Rb, Th, and LREE, but strong depletion of Nb-Ta-Ti and P, and high Rb/Sr ratio, indicating a crustal source (Rubatto and Hermann, 2003). All the evidence implies that these biotite granites were probably derived by partial melting of metaigneous rocks. Considering that the rocks have low Mg-number ($Mg^{\#}$ = 34–36) and compatible element contents (e.g., Ni and Cr), we inferred that significant mantle materials were not involved in forming the biotite granites.

The absence of significantly negative Eu anomalies indicates that the source was plagioclase-free due to the high partition coefficient (*D*) of Eu (D_{Eu} = 5.417) between felsic melts and plagioclase (Nash and Crecraft, 1985). All the samples are strongly enriched in LREE with high $(La/Yb)_N$ of 41–61 and exhibit steep HREE patterns with $(Gd/Yb)_N$ of 2.0–2.9, indicating the presence of garnet in the source. Previous studies indicate that during the dehydration-melting of meta-igneous rocks (biotite gneiss and quartz amphibolite), garnet would occur as one of residual phases at pressures ⩾ 12.5 kbar and plagioclase would be unstable at pressures ⩾ 15 kbar (Douce et al., 1995). The occurrence of garnet without plagioclase indicates that the source of the biotite granites is relatively deep (> 50 km). In summary, the biotite granites were likely produced by partial melting of meta-igneous rocks within the thickened lower crust (> 50 km).

6.2 Tectonic implications

In recent years, based on comprehensive studies on ophiolites, magmatism, structure geology, sedimentary rocks, and HV/EHV metamorphic rocks (Zonenshain et al., 1990; Chen and Jahn, 2004; Gao et al., 2007; Zhang et al., 2007; Hegner et al., 2010), knowledge about the tectonic evolution of the CAOB has been tremendously improved. However, granitoids from each tectonic unit have been interpreted to be emplaced in different tectonic settings, and their tectonic implications remain unclear and controversial (Kozakov et al., 1997; Budnikov et al., 1999; Yarmolyuk et al., 2002; Jahn et al., 2004, 2009; Annikova et al., 2006; Orolmaa et al., 2008).

Using 227 Ma as the dividing line, the early Mesozoic granitoids of the CAOB were emplaced in two magmatic episodes (Li et al., 2010) (Fig. 1). In the western Baikal orogen, the first-stage magmatic rocks (251–227 Ma, alkaline A-type granites) were emplaced in a post-orogenic or intraplate tectonic setting (Yarmolyuk et al., 2002; Jahn et al., 2004, 2009). In the Altai orogen, the first-stage granites consist of post-orogenic I-type and A-type

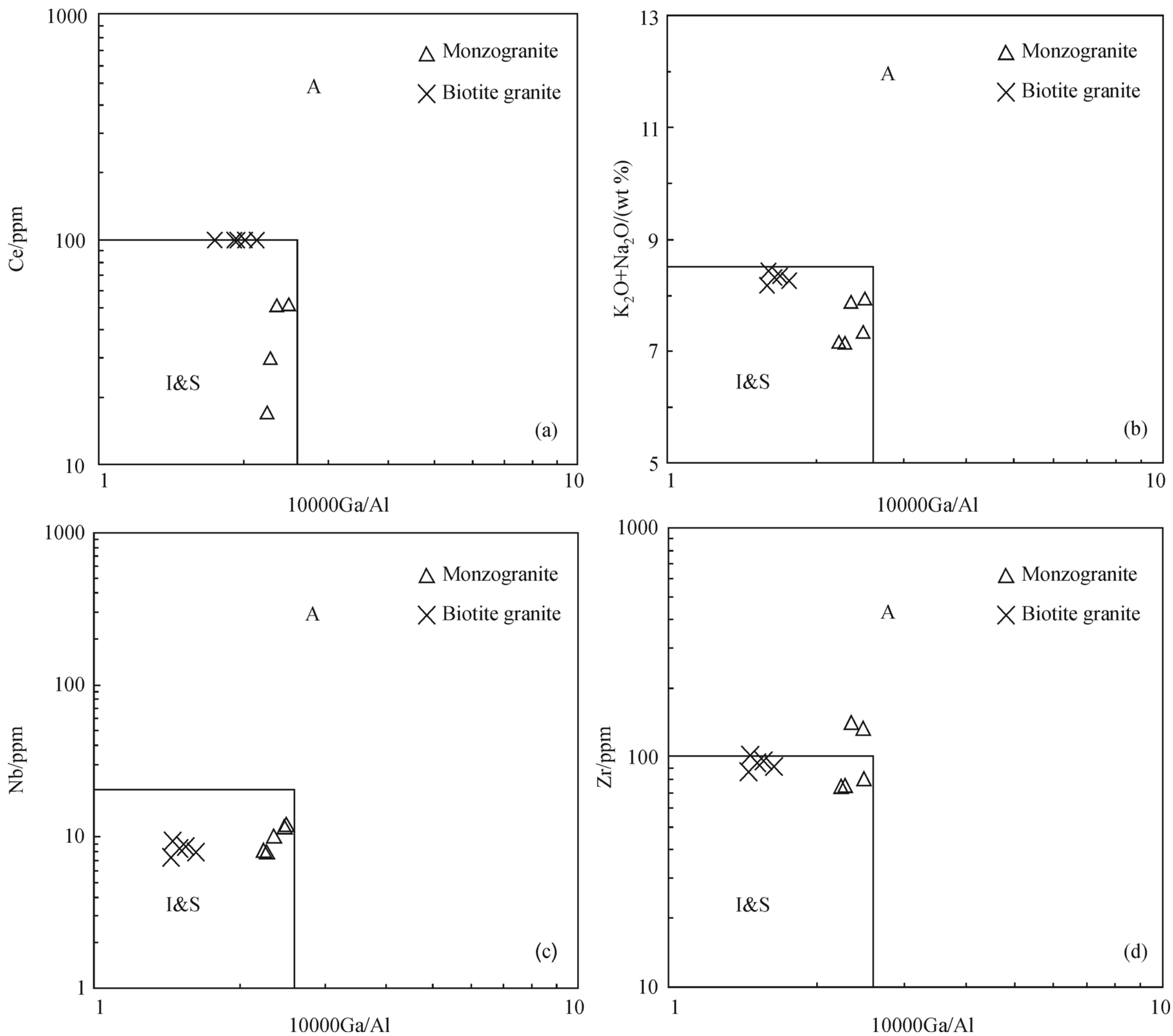

Fig. 12 Diagrams of Ce (a), Zr (b), Nb (c), and ($Na_2O + K_2O$) (d) vs. 10000 × Ga/Al (after Whalen et al., 1996).

granites, and most scholars believed that the main orogenic event ended during the Late Permian (Fig. 1; Pavlova et al., 2008). In the eastern Tianshan and Beishan orogens, the first-stage granites are composed of high-K calc-alkaline A-type and I-type granites, emplaced in a post-collision tectonic setting (Fig. 1; Li et al., 2006a; Zhang et al., 2007; Wang et al., 2008b; Li et al., 2010; Wang et al., 2010; Zhou et al., 2010; Zhang et al., 2013). However, in the middle of Mongolia, the first-stage granites are high-K calc-alkaline and calc-alkaline S- and I-type granites, formed in a late syn-orogenic setting (Orolmaa et al., 2008) (Fig. 1). In the Inner Mongolia and Jilin orogen, the first-stage granites consist of high-K calc-alkaline I-type and S-type granites with arc affinities (Fig. 1) (Tao et al., 2003; Bao et al., 2007; Li et al., 2007; Miao et al., 2008; Zhang et al., 2008; Chen et al., 2009; Zhang, 2009; Tong et al., 2010a).

The second stage ranged from Late Triassic to Early Jurassic (226–195 Ma). These magmatic rocks include high-K calc-alkaline A-type granites and I-type granites, formed in a post-orogenic tectonic setting or an extensional environment (Vladimirov et al., 2001; Tao et al., 2003; Shi et al., 2004; Annikova et al., 2006; Ma et al., 2007; Wang et al., 2007c, 2008a; Li et al., 2010) (Fig. 1). However, granites in the Okhotsk belt and adjacent Mongolia were emplaced in a syn-orogenic tectonic setting. Their emplacement might be in response to Mesozoic back-arc basin closure and arc-continent collision (Yarmolyuk et al., 2002; Jahn et al., 2004, 2009). Therefore, the two-stage granitoids from different tectonic units were emplaced in different tectonic environments.

Abundant Early Permian granites also intruded into the Alxa metamorphic basement, indicating that the studied area was strongly modified by the late Paleozoic orogeny (Geng and Zhou, 2012). Based on the spatial and temporal distribution of the Paleozoic granites, ophiolite-complex rocks, and volcanic-sedimentary assemblage, we believe that the late Paleozoic Enger Us ophiolitic belt (~302 Ma for pillow lava; Zheng et al., 2014), Shalazhashan granite (continental margin arc), and Chaganchulu ophiolitic belt (~275 Ma for gabbro; Zheng et al., 2014) made up a trench-arc-basin system as a product of the Paleo-Asian Oceanic southward subduction. Xie et al. (2014) have found some radiolarian fossils as young as the Late Permian, implying that the subduction of the Enger Us ocean might have lasted to at least the Late Permian. Furthermore, the ca. 250 Ma Wuliji post-collisional granite intruded into the upper section of the Late Permian, which is molasse formation composed of sandstone, gravel-bearing sandstone, silty shale, and conglomerate (Zhang et al., 2013). Thus, the Paleo-Asian branch ocean, represented by the Enger Us ophiolitic belt, was probably closed at the end of the Permian.

The quartz diorites (adakites) (~302 Ma) in this study are close to the southern Chaganchulu ophiolitic belt. As indicated by the petrogenesis of the quartz diorites, they likely originated from a subducted slab. Given the temporal and spatial distribution of the Chaganchulu ophiolitic belt and quartz diorites, we suggest that the quartz diorites might be derived by partial melting of the Chaganchulu back-arc oceanic slab. In the Langshan area, eastern Alxa block, some 292–285 Ma deformed granitic-granodioritic porphyries show typical arc affinities and might have been emplaced before the collision of the Zongnaishan-Shalazhashan arc with the Alxa block (Lin et al., 2014). Similarly, Feng et al. (2013) have investigated some 306–262 Ma, EW-trending mafic-ultramafic rocks which occurred in the Bijiertai, Honggueryulin, and Qinggele areas along the Bayinnuoergong-Langshan tectonic belt. All the mafic-ultramafic rocks represent arc magmatism as products of the Chaganchulu back-arc oceanic subduction. At ca. 246.5 Ma, the emplacement of the tonalites with arc affinities implied a subduction setting rather than a collisional or post-collisional setting. The Chaganchulu oceanic continued to the Early Triassic.

Considering the location and age of the Enger Us and Hegenshan ophiolitic belt, the Enger Us oceanic basin might be equivalent to the Hegenshan ocean which was also closed not later than the Permian (Fig. 1; Miao et al., 2008). Similarly, another Paleo-Asian branch ocean, represented by the Suolunshan-Xilamulun suture zone, might be equivalent to the Chaganchulu back-arc oceanic basin, which was closed in the late Permian-early Triassic, consistent with the final amalgamation of the Sino-Korean and Siberian cratons (Wang and Fan, 1997; Li et al., 2006b; Li et al., 2007; Tong et al., 2010b).

From 235 Ma to 229.5 Ma, partial melting of the continental lower crust produced the monzogranites and biotite granites. In the tectonic discrimination diagrams of granites (Fig. 13), all the samples are plotted within the post-collision field (Pearce et al., 1984). It is then inferred that the area might have undergone tectonic transformation from a collisional orogenic compressional environment to a post-orogenic extensional environment.

On the basis of the new petrological, geochemical, and geochronologic data, together with studies on regional geology, we propose an integrated model for the Late Paleozoic to Early Mesozoic tectonic evolution of the Alxa block as illustrated in Fig. 14:

1) Southward subduction of the Paleo-Asian Ocean produced a trench-arc-basin system (Southern Mongolian Ocean + Zongnaishan-Shalazhashan island arc + Chaganchulu back-arc basin) (Fig. 14(a)).

2) From 302 Ma to Late Permian, the Chaganchulu back-arc oceanic slab subducted south underneath the Alxa block (Feng et al., 2013; Lin et al., 2014; Zheng et al., 2014), and partial melting of the subducted slab produced the quartz diorites with adakitic affinities (Fig. 14(b)).

3) From Late Permian to 240 Ma, the southward subducted slab-released fluids induced partial melting of the overlying enriched mantle wedge. Then, fractional

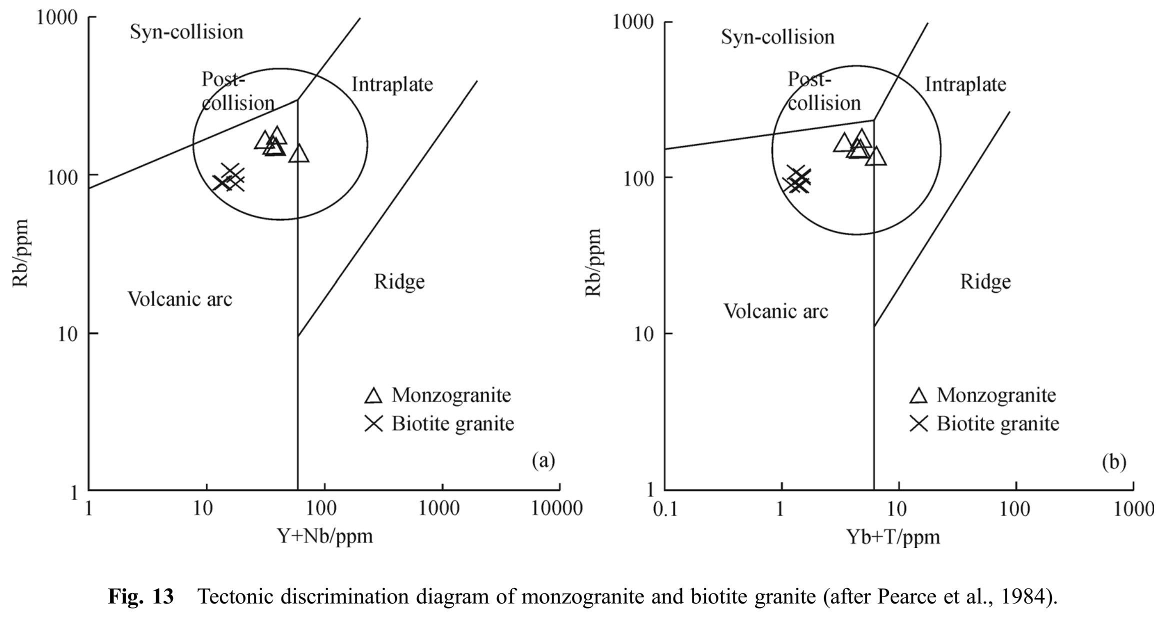

Fig. 13 Tectonic discrimination diagram of monzogranite and biotite granite (after Pearce et al., 1984).

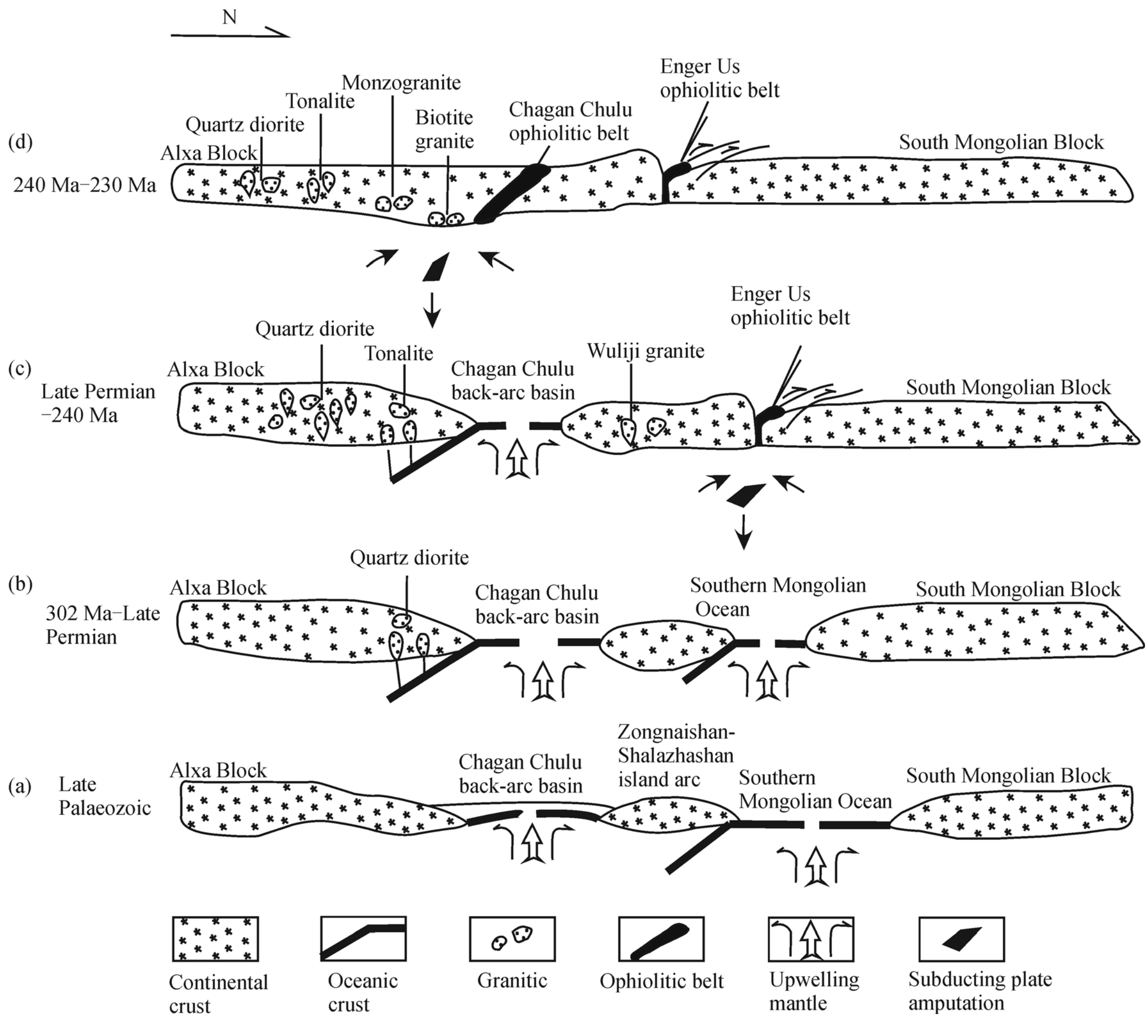

Fig. 14 Tectonic evolution sketch of the Alxa region (after Zhang et al., 2013; Xie et al., 2014; Zheng et al., 2014; Xiao et al., 2015).

crystallization of the modified mantle-derived basaltic magmas produced the tonalites (Fig. 14(c)). In this period, the Enger Us oceanic basin was closed due to the collision of South Mongolian Block with the Zongnaishan-Shalazhashan arc (Xie, 2014; Zheng et al., 2014; Xiao et al., 2015).

4) From 240 Ma to 230 Ma, the Chaganchulu back-arc basin was finally closed and the Zongnaishan-Shalazhashan island arc was welded to the Alxa block, followed by crustal thickening. Then, asthenosphere mantle upwelling triggered by the slab break-off induced partial melting of the thickened lower crust to produce the biotite granites and partial melting of relatively thin crust to form the monzogranites, respectively (Fig. 14(d)).

7 Conclusions

1) The quartz diorites (302±9.2 Ma) were derived by partial melting of the initially subducted Chaganchulu back-arc oceanic slab, The tonalites (246.5±4.6 Ma) were produced by fractional crystallization of a modified lithospheric mantle-derived basaltic magma, and were formed in a volcanic arc setting. The monzogranites (235±4.4 Ma) had a crustal source, and coeval basaltic magmas were required for triggering partial melting of the crustal source. The biotite granites (229.5±5.6 Ma) were derived by partial melting of meta-igneous rocks within the thickened lower crust.

2) The Enger Us oceanic basin was likely closed in the Late Permian, and the Chaganchulu back-arc oceanic basin began to subduct underneath the Alxa block at 302 Ma. This subduction process continued to the Early Triassic (246 Ma) and the basin closed fully before the Middle Triassic (235 Ma). The compressional environment led to crustal thickening. Then the asthenosphere mantle upwelling was triggered by slab breakoff and mantle-derived magma underplating near the crust-mantle boundary (240–230 Ma). The tectonic environment then converted to a post-orogenic extensional environment, and the area might also have undergone a conversion process from crustal thickening to thinning.

Acknowledgements During the research work, we appreciated advice from Senior Engineer Yang Bin of the Gansu Province Geology and Mining Bureau and Zhang Xiang, Engineer, of Gansu Province Geological Survey. We thank the editors and anonymous reviewers for comments that greatly improved the presentation of the paper. Thanks to Shuangshuang Wang for the help during the laboratory work. This study was supported by the National Natural Science Foundation of China (Grant No. 41173014), the Central Universities Fundamental Research Project (Lzu-Jbky-2012-128), and Gansu Key Laboratory of Mineral Resources in Western China (Lanzhou University) funded project.

References

Annikova I Y, Vladimirov A G, Vystavnoi S A (2006). U-Pb, $^{39}Ar/^{40}Ar$ age determination and Sm-Nd, Pb-Pb isotope data for the Kalgut a Mo-W ore-magmatic system (South Altai, Russia). Петрология, 14 (1): 90–108 (in Russian)

Atherton M P, Petford N (1993). Generation of sodium-rich magmas from newly underplated basaltic crust. Nature, 362(6416): 144–146

Bao Q Z, Zhang C J, Wu Z L, Wang H, Li W, Sang J H, Liu Y S (2007). Zircon SHRIMP U-Pb dating of granitoids in a Late Paleozoic rift area, southeastern Inner Mongolia, and its implications. Geology in China, 34(5): 790–798 (in Chinese)

Belousova E, Griffin W L, O'Reilly S Y, Fisher N L (2002). Igneous zircon: trace element composition as an indicator of source rock type. Contrib Mineral Petrol, 143(5): 602–622

Budnikov S V, Kovalenko V I, Kotov A B (1999). The age and sources of the Hangay batholiths (Central Mongolia), in: IGCP-420. Continental Growth in the Phanerozoic: Evidence from Central Asia. Rennes: Second workshop. Abstracts and Excursion Guidebook Geosciences, 11–12

Castillo P R, Janney P E, Solidum R U (1999). Petrology and geochemistry of Camiguin Island, southern Philippines: insights to the source of adakites and other lavas in a complex arc setting. Contrib Mineral Petrol, 134(1): 33–51

Chappell B W, White A J R (1974). Two contrasting granite type. Pacific Geology, 8:173–174

Charvet J, Shu L S, Laurent-Charvet S (2007). Paleozoic structural and geodynamic evolution of eastern Tianshan (NW China): welding of the Tarim and Junggar plates. Episodes, 30(3): 162–186

Charvet J, Shu L S, Laurent-Charvet S, Wang B, Faure M, Cluzel D, Chen Y, De Jong K (2011). Palaeozoic tectonic evolution of the Tianshan belt, NW China. Science China Earth Sciences, 54(2): 166–184

Chen B, Jahn B M (2004). Genesis of post-collisional granitoids and basement nature of the Junggar Terrane, NW China: Nd-Sr isotope and trace element evidence. J Asian Earth Sci, 23(5): 691–703

Chen B, Jahn B M, Tian W (2009). Evolution of the Solonker suture zone: constraints from zircon U-Pb ages, Hf isotopic ratios and whole-rock Nd-Sr isotope compositions of subduction and collision related magmas and forearc sediments. J Asian Earth Sci, 34(3): 245–257

Chen C M, Lu H F, Jia D, Cai D S, Wu S M (1999). Closing history of the southern Tianshan oceanic basin, western China: an oblique collisional orogeny. Tectonophysics, 302(1–2): 23–40

Defant M J, Maury R C, Ripley E M, Feigenson M D, Jacques D (1991). An example of island-arc petrogenesis: geochemistry and petrology of the southern Luzon arc, Philippines. J Petrol, 32(3): 455–500

Douce A E P, Beard J S (1995). Dehydration-melting of biotite gneiss and quartz amphibolite from 3 to 15 kbar. J Petrol, 36(3): 707–738

Drummond M S, Defant M J (1990). A model for trondhjemite-tonalite-dacite genesis and crustal growth via slab melting: Archean to modern comparisons. Journal of Geophysical Research: Solid Earth (1978–2012), 95 (B13): 21503–21521

Drummond M S, Defant M J, Kepezhinskas P K (1996). Petrogenesis of slab-derived trondhjemite-tonalite- dacite/adakite magmas. Trans R Soc Edinb Earth Sci, 87(1–2): 205–215

Feng J Y, Xiao W J, Windley B, Han C M, Wan B, Zhang J E, Ao S J, Zhang Z Y, Lin L N (2013). Field geology, geochronology and geochemistry of mafic–ultramafic rocks from Alxa, China: implications for Late Permian accretionary tectonics in the southern Altaids. J Asian Earth Sci, 78: 114–142

Gao J, John T, Klemd R, Xiong X M (2007). Mobilization of Ti-Nb-Ta during subduction: evidence from rutile-bearing dehydration segregations and veins hosted in eclogite, Tianshan, NW China. Geochim Cosmochim Acta, 71(20): 4974–4996

Gao J, Klemd R (2003). Formation of HP-LT rocks and their tectonic implications in the western Tianshan Orogen, NW China: geochemical and age constraints. Lithos, 66(1–2): 1–22

Gao J, Li M S, Xiao X C, Tang Y Q, He G Q (1998). Paleozoic tectonic evolution of the Tianshan Orogen, northwestern China. Tectonophysics, 287(1): 213–231

Gao J, Long L, Klemd R, Qian Q, Liu D, Xiong X, Su W, Liu W, Wang Y, Yang F (2009). Tectonic evolution of the South Tianshan orogen and adjacent regions, NW China: geochemical and age constraints of granitoid rocks. Int J Earth Sci, 98(6): 1221–1238

Ge X H, Ma W P, Liu J L, Ren S M, Liu Y J, Yuan S H, Wang M P (2009). A discussion on the tectonic framework of Chinese mainland. Geology in china, 36 (5): 949–965 (in Chinese)

Geng Y S, Wang X S, Shen Q H, Wu C M (2007). Chronology of the Precambrian metamorphic series in the Alxa area, Inner Mongolia. Geology in China., 34(2): 251–261 (in Chinese)

Geng Y S, Zhou X W (2010). Early Neoproterozoic granite events in Alxa area of Inner Mongolia and their geological significance: evidence from geochronology. Acta Petrologica et Mineralogical, 29 (6): 779–795

Geng Y S, Zhou X W (2011). Characteristics of geochemistry and zircon Hf isotope of the Early Neoproterozoic granite in Alxa area, Inner Mongolia. Acta Petrologica Sinica, 27(4): 897–908

Geng Y S, Zhou X W (2012). Early Permian magmatic events in the Alxa metamorphic basement: evidence from geochronology. Acta Petrologica Sinica, 28(9): 2667–2685

Gong J H, Zhang J X, Yu S Y (2013). Redefinition of the Longshoushan Group outcropped in the eastern segment of Longshoushan on the southern margin of Alxa Block: evidence from detrital zircon U-Pb dating results. Acta Petrologica et Mineralogical., 32(1): 1–22

Gong J H, Zhang J X, Yu S Y, Li H K, Hou K J, (2012). 2.5 Ga TTG rocks in the western Alxa Block and their implications. Chin Sci Bull, 57(31): 4064–4076

Govindaraju G (1994). Compilation of working values and sample description for 383 geostandards. Geostand Newsl, 18: 1–158

Han B F, Guo Z J, He G Q (2010a). Timing of major suture zones in North Xinjiang, China: constraints from stitching plutons. Acta

Petrologica Sinica, 26(8): 2233–2246

Han B F, Guo Z J, Zhang Z C, Zhang L, Chen J F, Song B (2010b). Age, geochemistry, and tectonic implications of a late Paleozoic stitching pluton in the North Tian Shan suture zone, western China. Geol Soc Am Bull, 122(3–4): 627–640

Han B F, He G Q, Wang X C, Guo Z J (2011). Late Carboniferous collision between the Tarim and Kazakhstan-Yili terranes in the western segment of the South Tian Shan Orogen, Central Asia, and implications for the Northern Xinjiang, western China. Earth Sci Rev, 109(3–4): 74–93

Han B F, Zhang C, Zhao L, Ren R, Xu Z, Chen J f, Zhang L, Zhou Y Z, Song B (2010c). A preliminary study of granitoids in western Inner Mongolia. Acta Petrologica et Mineralogical, 29(6): 741–749

Hegner E, Klemd R, Kröner A, Corsini M, Alexeiev D V, Iaccheri L M, Zack T, Dulski P, Xia X, Windley B F (2010). Mineral ages and PT conditions of Late Paleozoic high-pressure eclogite and provenance of mélange sediments from Atbashi in the south Tianshan orogen of Kyrgyzstan. Am J Sci, 310(9): 916–950

Hou Z Q, Gao Y F, Meng X J, Qu X M, Huang W (2004). Genesis of adakitic porphyry and tectonic controls on the Gangdese Miocene Porphyry copper belt in the Tibetan orogen. Acta Petrologica Sinica, 20(2): 239–248

Jahn B M, Capdevila R, Liu D, Vernon A, Badarch G (2004). Sources of Phanerozoic granitoids in the transect Bayanhongor-Ulaan Baatar, Mongolia: geochemical and Nd isotopic evidence, and implications for Phanerozoic crustal growth. J Asian Earth Sci, 23(5): 629–653

Jahn B M, Litvinovsky B A, Zanvilevich A N, Reichow M (2009). Peralkaline granitoid magmatism in the Mongolian Transbaikalian Belt: evolution, petrogenesis and tectonic significance. Lithos, 113 (3–4): 521–539

Kay S M, Mpodozis C (2001). Central Andes ore deposits linked to evolving shallow subduction systems and thickening crust. GSA Today, 11(3): 4–9

Kay S M, Ramos V A, Marquez M (1993). Evidence in Cerro Pampa volcanic rocks for slab-melting prior to ridge-trench collision in southern South America. J Geol, 101(6): 703–714

Kozakov I K, Bibikova E V, Kovalenko V I (1997). U-Pb Age of Granitoids Located within the Southern Slope of the Caledonides, Mongolian Altai. Dokl Earth Sci, 353a: 338–340

Li D P, Chen Y L, Wang Z, Lin Y, Zhou J (2012). Paleozoic sedimentary record of the Xing-Meng Orogenic Belt, Inner Mongolia: implications for the provenances and tectonic evolution of the Central Asian Orogenic Belt. Chin Sci Bull, 57(7): 776–785

Li H Q, Chen F W, Li J Y, Qu W J, Wang D H, Wu H, Deng G, Mei Y P (2006a). Age of mineralization and host rocks in the Baishan rhenium-molybdenum district, East Tianshan, Xinjiang, China: revisited. Geological Bulletin of China, 25(8): 916–922

Li J Y, Gao L M, Sun G H (2007). Shuangjingzi middle Triassic syn-collisional crust-derived granite in the east Inner Mongolia and its constraint on the timing of collision between Siberian and Sino-Korean paleo-plates. Acta Petrologica Sinica, 23(3): 565–582

Li J Y, Yang T N, Li Y P, Zhu Z X (2009). Geological features of the Karamaili faulting belt, eastern Junggar region, Xinjiang, China and its constraints on the reconstruction of Late Paleozoic ocean-continental framework of the Central Asian region. Geological Bulletin of China, 28(12): 1817–1826

Li P W, Gao R, Guan Y, Li Q S (2006b). Palaeomagnetic constraints on the final closure time of Solonker Linxi Suture. Journal of Jilin University (Earth Science Edition), 36(5): 744–758

Li S, Wang T, Tong Y (2010). Spatial-temporal distribution and tectonic settings of Early Mesozoic granitoids in the middle south segment of the Central Asia Orogenic System. Acta Petrologica et Mineralogica, 29(6): 642–662

Li X H (1997). Geochemistry of the Longsheng ophiolite from the southern margin of Yangtze craton, SE China. Geochem J, 31(5): 323–337

Li Y J, Sun L D, Wu H R, Zhang G Y, Wang G L, Huang Z B (2005). Permo-Carboniferous Radiolarians from the Wupata'erkan Group, Western South Tianshan, Xinjiang, China. Acta Geologica Sinica-English Edition, 79(1): 16–23

Li Y J, Wang Z M, Wu H R, Hang Z B, Tan Z J, Luo J C (2002). Discovery of Radiolarian Fossils from the Aiketik Group at the western end of the South Tianshan Mountains of China and its implications. Acta Geologica Sinica-English Edition, 76(2): 146–154

Lin L, Xiao W, Wan B, Windley B, Ao S, Han C, Feng J, Zhang J, Zhang Z (2014). Geochronologic and geochemical evidence for persistence of south-dipping subduction to late Permian time, Langshan area, Inner Mongolia (China): significance for termination of accretionary orogenesis in the southern Altaids. Am J Sci, 314(2): 679–703

Liu J F, Chi X G, Zhang X Z, Ma Z H, Zhao Z, Wang T F, Hu Z C, Zhao X Y (2009). Geochemical characteristic of carboniferous quartz-diorite in the southern Xiwuqi area, Inner Mongolia and its tectonic significance. Acta Geol Sin, 83(3): 365–376 (in Chinese)

Liu Y, Liu X M, Hu Z C, Diwu C R, Yuan H L, Gao S (2007). Evaluation of accuracy and long-term stability of determination of 37 trace elements in geological samples by ICP-MS. Acta Petrologica Sinica, 23(5): 1203–1210

Ma Y S, Zeng Q L, Song B, Du J J, Yang F Q, Zhao Y (2007). SHRIMP U-Pb dating of zircon from Panshan granitoid pluton in Yanshan orogenic belt and its tectonic implications. Acta Petrologica Sinica, 23(3): 547–556

Macpherson C G, Dreher S T, Thirlwall M F (2006). Adakites without slab melting: high pressure differentiation of island arc magma, Mindanao, the Philippines. Earth Planet Sci Lett, 243(3–4): 581–593

Maniar P D, Piccoli P M (1989). Tectonic discrimination of granitoids. Geol Soc Am Bull, 101(5): 635–643

Mao Q, Xiao W, Fang T, Wang J, Han C, Sun M, Yuan C (2012). Late Ordovician to early Devonian adakites and Nb-enriched basalts in the Liuyuan area, Beishan, NW China: implications for early Paleozoic slab-melting and crustal growth in the southern Altaids. Gondwana Res, 22(2): 534–553

Martin H (1999). Adakitic magmas: modern analogues of Archaean granitoids. Lithos, 46(3): 411–429

Miao L C, Fan W M, Liu D Y, Zhang F Q, Shi Y R, Guo F (2008). Geochronology and geochemistry of the Hegenshan ophiolitic complex: implications for late-stage tectonic evolution of the Inner Mongolia-Daxinganling Orogenic Belt, China. J Asian Earth Sci, 32 (5–6): 348–370

Middlemost E A K (1985). Magmas and Magmatic Rocks. London: Longman, 1–266

Muir R J, Weaver S D, Bradshaw J D, Eby G N, Evans J A (1995). The Cretaceous Separation Point batholith, New Zealand: granitoid magmas formed by melting of mafic lithosphere. J Geol Soc London, 152(4): 689–701

Nash W P, Crecraft H R (1985). Partition coefficients for trace elements in silicic magmas. Geochim Cosmochim Acta, 49(11): 2309–2322

Orolmaa D, Erdenesaihan G, Borisenko A S, Fedoseev G S, Babich V V, Zhmodik S M (2008). Permian Triassic granitoid magmatism and metallogeny of the Hangayn (central Mongolia). Russ Geol Geophys, 49(7): 534–544

Pavlova G G, Borisenko A S, Goverdovskii V A, Travin A V, Zhukova I A, Tret'yakova I G (2008). Permian Triassic magmatism and Ag-Sb mineralization in southeastern Altai and northwestern Mongolia. Russ Geol Geophys, 49(7): 545–555

Pearce J A, Harris N B W, Tindle A G (1984). Trace element discrimination diagrams for the tectonic interpretation of granitic rocks. J Petrol, 25(4): 956–983

Peccerillo R, Taylor S R (1976). Geochemistry of Eocene calcalkaline volcanic rocks from the Kastamonu area, Northern Turkey. Contrib Mineral Petrol, 58(1): 63–81

Rapp R P (1997). Heterogenous source regions for Archean granitoids. In: Wit M J, Ashwal L D, eds. Greenstone Belt. Oxford: Oxford University Press, 35–37

Rapp R P, Shimizu N, Norman M D, Applegate G (1999). Reaction between slab-derived melts and peridotite in the mantle wedge: experimental constraints at 3.8 GPa. Chem Geol, 160(4): 335–356

Richards J P, Kerrich R (2007). Special paper: adakite-like rocks: their diverse origins and questionable role in metallogenesis. Econ Geol, 102(4): 537–576

Rubatto D, Hermann J (2003). Zircon formation during fluid circulation in eclogites (Monviso, Western Alps): implications for Zr and Hf budget in subduction zones. Geochim Cosmochim Acta, 67(12): 2173–2187

Sen C, Dunn T (1994). Dehydration melting of a basaltic composition amphibolites at 1.5 and 2.0 GPa: implications for the origin of adakite. Contrib Mineral Petrol, 117(4): 394–409

Shi Y R, Liu D Y, Zhang Q, Jian P, Zhang F Q, Miao L C, Shi G H, Zhang L Q, Tao H (2004). SHRIMP dating of diorites and granites in southern Suzuoqi, Inner Mongolia. Acta Geol Sin, 78(6): 789–799

Song S, Niu Y, Su L, Xia X (2013). Tectonics of the North Qilian orogen, NW China. Gondwana Res, 23(4): 1378–1401

Sun S S, McDonough W F (1989). Chemical and isotopic systematics of oceanic basalts: implications for mantle composition and processes. In: Saunders A D, Norry M J, eds. Magmatism in the Ocean Basins. Geological Society Special Publication, 42: 313–345

Tao J X, Hu F X, Chen Z Y (2003). Characteristics and tectonic setting of Indosinian S-type granites in the northern margin of North China landmass. Acta Petrologica et Mineralogical, 20(2): 112–118

Tian Z, Xiao W, Shan Y, Windley B, Han C, Zhang J E, Song D (2013). Mega-fold interference patterns in the Beishan orogen (NW China) created by change in plate configuration during Permo-Triassic termination of the Altaids. J Struct Geol, 52: 119–135

Tian Z, Xiao W, Sun J, Windley B F, Glen R, Han C, Zhang Z, Zhang J, Wan B, Ao S, Song D (2015). Triassic deformation of Permian Early Triassic arc-related sediments in the Beishan (NW China): last pulse of the accretionary orogenesis in the southernmost Altaids. Tectonophysics, 662: 363–384

Tong Y, Hong D W, Wang T (2010a). Spatial and temporal distribution of granitoids in the middle segment of the Sino-Mongolian Border and its tectonic and metallogenic implications. Acta Geoscientica Sinica, 31(3): 395–412

Tong Y, Wang T, Hong D W, Han B F, Zhang J J, Shi X J, Wang C (2010b). Spatial and temporal distribution of the Carboniferous-Permian granitoids in northern Xinjiang and its adjacent areas, and its tectonic significance. Acta Petrologica et Mineralogica, 29(6): 619–641

Vladimirov A G, Kozlov M S, Shokalskii S P (2001). Major epochs of intrusive magmatism of Kuznetsk Alatau, Altai and Kalba (from U-Pb isotope dates). Geologiyai Geofizika, 42(8): 1157–1178 (Russian Geology and Geophysics)

Vladimirov A G, Kruk N N, Polyanskii O P (2005). Correlation of Hercynian deformations, sedimentation and magmatism in the Altai collisional system as reflecting plate and plume tectonics. Problem of Tectonic of the Central Asia. Moscow: Geos. P., 1277–1308

Wang B, Shu L S, Cluzel D, Faure M, Charvet J (2007a). Geochemical constraints on Carboniferous volcanic rocks of the Yili Block (Xinjiang, NW China): implication for the tectonic evolution of Western Tianshan. J Asian Earth Sci, 29(1): 148–159

Wang B, Shu L, Faure M, Jahn B, Cluzel D, Charvet J, Chung S, Meffre S (2011). Paleozoic tectonics of the southern Chinese Tianshan: insights from structural, chronological and geochemical studies of the Heiyingshan ophiolitic mélange (NW China). Tectonophysics, 497 (1): 85–104

Wang Q, Wyman D A, Zhao Z H, Xu J F, Bai Z H, Xiong X L, Dai T M, Li C F, Chu Z Y (2007b). Petrogenesis of Carboniferous adakites and Nb-enriched arc basalts in the Alataw area, northern Tianshan range (western China): implications for Phanerozoic crustal growth in the central Asia orogenic belt. Chem Geol, 236(1–2): 42–64

Wang Q, Xu J F, Jian P, Bao Z W, Zhao Z H, Li C F, Ma J L (2006). Petrogenesis of adakitic porphyries in an extensional tectonic setting, Dexing, South China: implications for the genesis of porphyry copper mineralization. J Petrol, 47(1): 119–144

Wang T Y, Gao J P, Wang J R (1998a). Magmatism of collisional and post-orogenic period in northern Alexa region in Inner Mongolia. Acta Geol Sin, (02): 126–137

Wang T Y, Wang J R, Liu J K (1994). Igneous rock associations and geochemical characteristics of volcanic arc with continental crustal basement in Zongnaishan-Shalazhashan. Geochimica, 23(S1): 162–172

Wang T Y, Zhang M J, Wang J R, Gao J P (1998b). The characteristics and tectonic implications of the thrust belt in Eugerwusu, China. Scientia Geologica Sinica, 33(04): 385–394

Wang T, Jahn B M, Kovach V P (2008a). Mesozoic anorogenic granitic magmatism in the Altai Paleozoic accretionary orogen, NW China, and its implications for crustal architecture and growth. Abstract SE 53-A010, AOGS 5th Annual General Meeting, Busan, Korea

Wang T, Tong Y, Jahn B M (2007c). SHRIMP U-Pb Zircon geochronology of the Altai No.3 Pegmatite , NW China, and its implications for the origin and tectonic setting of the pegmatite. Ore Geol Rev, 32: 325–336

Wang T, Zheng Y D, Li T B, Gao Y (2004). Mesozoic granitic magmatism in extensional tectonics near the Mongolian border in China and its implications for crustal growth. J Asian Earth Sci, 23 (5): 715–729

Wang Y J, Fan Z Y (1997). Discovery of Permian radiolarians in ophiolite belt on northern side of Xarmoron river, Nei Monggol and its geological significance. Acta Palaeontologica Sin, 36(1): 58–69

Wang Y W, Wang J B, Wang L J, Long L L (2008b). Zircon U-Pb age, Sr-Nd isotope geochemistry and geological significances of the Weiya mafic-ultramafic complex, Xinjiang. Acta Petrologica Sinica, 24(4): 781–792

Wang Y, Sun G H, Li J Y (2010). U-Pb (SHRIMP) and $^{40}Ar/^{39}Ar$ geochronological constraints on the evolution of the Xingxingxia shear zone, NW China: a Triassic segment of the Altyn Tagh fault system. Geol Soc Am, 122(3–4): 487–505

Whalen J B, Jenner G A, Longstaffe F J, Robert F, Gariépv C (1996). Geochemical and isotopic (O, Nd, Pb and Sr) constraints on A-type granite: petrogenesis based on the Topsails igneous suite, Newfoundland Appalachians. J Petrol, 37(6): 1463–1489

Wilson M (1989). Igneous Petrogenesis. London: Allen and Unwin, 120–158

Wu T R, He G Q (1993). Tectonic units and their fundamental characteristics on the northern margin of the Alxa block. Acta Geol Sin, 67(2): 97–108

Xia L Q, Xu X Y, Xia Z C, Li X M, Ma Z P, Wang L S (2004). Petrogenesis of Carboniferous rift-related volcanic rocks in the Tianshan, northwestern China. Geol Soc Am Bull, 116(3): 419–433

Xiao W J, Han C, Yuan C, Sun M, Lin S, Chen H, Li Z, Li J, Sun S (2008). Middle Cambrian to Permian subduction-related accretionary orogenesis of Northern Xinjiang, NW China: implications for the tectonic evolution of central Asia. J Asian Earth Sci, 32(2–4): 102–117

Xiao W J, Huang B C, Han C M, Sun S, Li J L (2010a). A review of the western part of the Altaids: a key to understanding the architecture of accretionary orogens. Gondwana Res, 18(2–3): 253–273

Xiao W J, Mao Q G, Windley B F, Han C M, Qu J F, Zhang J E, Ao S J, Guo Q Q, Cleven N R, Lin S F, Shan Y H, Li J L (2010b). Paleozoic multiple accretionary and collisional processes of the Beishan orogenic collage. Am J Sci, 310(10): 1553–1594

Xiao W J, Windley B F, Allen M B, Han C (2013). Paleozoic multiple accretionary and collisional tectonics of the Chinese Tianshan orogenic collage. Gondwana Res, 23(4): 1316–1341

Xiao W J, Windley B F, Huang B C, Han C M, Yuan C, Chen H L, Sun M, Sun S, Li J L (2009). End-Permian to mid-Triassic termination of the accretionary processes of the southern Altaids: implications for the geodynamic evolution, Phanerozoic continental growth, and metallogeny of Central Asia. Int J Earth Sci, 98(6): 1189–1217

Xiao W J, Windley B F, Sun S, Li J, Huang B, Han C, Yuan C, Sun M, Chen H (2015). A tale of amalgamation of three Permo-Triassic collage systems in central Asia: oroclines, sutures, and terminal accretion. Annu Rev Earth Planet Sci, 43(1): 477–507

Xie F Q (2014). Study of granites rock mass of Zongnai, Shalaza and Bayinnuoergong. China University of Geosciences (Beijing)

Xie L, Yin H Q, Zhou H R, Zhang W J (2014). Permian radiolarians from the Engeerwusu suture zone in Alashan area, Inner Mongolia and its geological significance. Geological Bulletin of China, 33: 691–697 (in Chinese)

Xu B L, Yan G H, Lu F X, Zou T R, Tond Y, Cai J H, Liu C X, Zhang H F (2001). Petrology of rich-alkaline and alkaline intrusive complexes in Beishan-Alxa Region. Acta Petrologica et Mineralogica, 20(3): 263–272

Xu H J, Ma C Q (2003). Constraints of experimental petrology on the origin of adakites, and petrogenesis of Mesozoic K-rich and high Sr/Y ratio granitoids in eastern China. Earth Sci Front, 10: 417–427 (in Chinese)

Yang S H, Zhou M F (2009). Geochemistry of the 430 Ma Jingbulake mafic-ultramafic intrusion in Western Xinjiang, NW China: implications for subduction related magmatism in the South Tianshan orogenic belt. Lithos, 113(1–2): 259–273

Yarmolyuk V V, Kovalenko V I, Sal'nikova E B (2002). Tectono-magmatic zoning, magma sources and geodynamics of the early Mesozoic Mongolia-Transbaikal province. Geotectonics, 36(4): 293–311

Zhai M G, Bian A G (2000). At the end of the North China craton new super late Archean and Paleoproterozoic continent split a Mesoproterozoic cleavage. Sci China Ser D, 30(B12): 129–137

Zhang J, Li J Y, Liu J F (2011). The relationship between the Alxa Block and the North China Plate during the Early Paleozoic: new information from the Middle Ordovician detrital zircon ages in the eastern Alxa Block. Acta Petrologica Sinica, 28(9): 2912–2934

Zhang J, Wang T, Zhang L, Tong Y, Zhang Z, Shi X, Guo L, Huang H, Yang Q, Huang W, Zhao J, Ye K, Hou J (2015). Tracking deep crust by zircon xenocrysts within igneous rocks from the northern Alxa, china: constraints on the southern boundary of the central Asian orogenic belt. J Asian Earth Sci, 108: 150–169

Zhang L F, Ai Y L, Li Q, Li X P, Song S G, Wei C J (2005). The formation and tectonic evolution of UHP metamorphic belt in southwestern Tianshan, Xinjiang. Acta Petrologica Sinica, 21(4): 1029–1038

Zhang L F, Ai Y L, Li X P, Rubatto D, Song B, Williams S, Song S G, Ellis D, Liu J G (2007). Triassic collision of western Tianshan orogenic belt, China: evidence from SHRIMP U-Pb dating of zircon from HP/UHP eclogitic rocks. Lithos, 96(1–2): 266–280

Zhang Q, Jin W J, Li C D, Wang Y L (2010). Revisiting the new classification of granitic rocks based on whole-rock Sr and Yb contents: index. Acta Petrologica Sinica, 26(4): 985–1015

Zhang Q, Qian Q, Wang E Q, Wang Y, Zhao T P, Hao J, Guo G J (2001a). An east China plateau in mid-late Yanshanian period: implication from adakites. Chinese Journal of Geology, 36(2): 248–255

Zhang Q, Wang Y, Liu W, Wang Y L (2002a). Adakite: its characteristics and implications. Geological Bulletin of China, 21: 431–435 (in Chinese)

Zhang Q, Wang Y, Qian Q, Yang J H, Wang Y L, Zhao T P, Guo G J (2001b). The characteristics and tectonic-metallogenic significances of the adakites in Yanshan period from eastern China. Acta Petrologica Sinica, 17(2): 236–244

Zhang Q, Wang Y, Wang Y L (2001c). Preliminary study on the components of the lower crust in east China Plateau during Yanshanian Period: constraints on Sr and Nd isotopic compositions of adakite-like rocks. Acta Petrologica Sinica, 17(4): 505–513

Zhang W Y, Nie F J, Liu Y, Jiang S H, Xu D Q, Guo L J (2008). 40Ar-^{39}Ar Geochronology of the Aououte Cu-Zn Deposit in Inner-Mongolia and its Significance. Acta Geoscientica Sinica, 29(5): 592–598

Zhang W, Wu T R, Feng J C (2013). Time constraints for the closing of the Paleo-Asian Ocean in the Northern Alxa Region: evidence from Wuliji granites. Science China. Earth Sci, 56: 153–164

Zhang Y Q (2009). Geochemical characteristics of Permian adakitic granodiorite in Bayinwula of Sonid Left Banner, Inner Mongolia. Acta Petrologica et Mineralogica, 28(4): 329–338

Zhang Y Q, Han J G, Hu F X (2002b). Characteristics and tectonic significance of granites of Middle Triassic in Bayinnuorigong Area, Inner Mongolia. Inner Mongolia Geological, (4): 15–20

Zhang Y Y, Dostal J, Zhao Z H, Liu C, Guo Z J (2011). Geochronology, geochemistry and petrogenesis of mafic and ultramafic rocks from Southern Beishan area, NW China: implications for crust-mantle interaction. Gondwana Res, 20(4): 816–830

Zhang Z F, Li C Y, Niu Y Z (1997). Role, significance, characteristics and range of Alashan-Dunhuang land block. Inner Mongolia Geological, (2): 1–14

Zhao Q Y, Liu Z H, Wu X W, Chen X F (2007). Characteristics and origin of Halaheshao pluton in Da Qingshan region, Inner-Mongolia. J Mineral Petrol, 27(1): 46–51

Zheng R, Wu T, Zhang W, Xu C, Meng Q, Zhang Z (2014). Late Paleozoic subduction system in the northern margin of the Alxa block, Altaids: geochronological and geochemical evidences from ophiolites. Gondwana Res, 25(2): 842–858

Zhou T F, Yuan F, Zhang D Y, Fan Y, Liu S, Peng M X, Zhang J D (2010). Geochronology, tectonic setting and mineralization of granitoids in Jueluotage area, eastern Tianshan, Xinjiang. Acta Petrologica Sinica, 26(2): 478–502

Zonenshain L P, Kuzmin M I, Natapov L M, Page B M (1990). Geology of the USSR: A Plate-Tectonic Synthesis. American Geophysical Union, Geodynamics Series, 21: 1–242